PUBLICATIONS OF
THE UNIVERSITY OF EASTERN FINLAND

Dissertations in Forestry and Natural Sciences

UNIVERSITY OF
EASTERN FINLAND

PAAVO VARTIAINEN

ADVANCED METHODS FOR HUMAN MOTION ANALYSIS - APPLICATIONS TO GAIT AND SPINE BIOMECHANICS

UNIVERSITY OF
EASTERN FINLAND

PUBLICATIONS OF THE UNIVERSITY OF EASTERN FINLAND
DISSERTATIONS IN FORESTRY AND NATURAL SCIENCES

N:o 267

Paavo Vartiainen

ADVANCED METHODS FOR HUMAN MOTION ANALYSIS - APPLICATIONS TO GAIT AND SPINE BIOMECHANICS

ACADEMIC DISSERTATION

To be presented by the permission of the Faculty of Science and Forestry for public examination in the Auditorium SN200 in Snellmania Building at the University of Eastern Finland, Kuopio, on May 19th, 2017, at 12 o'clock.

University of Eastern Finland
Department of Applied Physics
Kuopio 2017

Grano Oy
Jyväskylä, 2017
Editors: Pertti Pasanen, Jukka Tuomela,
Pekka Toivanen, Matti Vornanen

Distribution:
University of Eastern Finland Library / Sales of publications
P.O. Box 107, FI-80101 Joensuu, Finland
julkaisumyynti@uef.fi
http://www.uef.fi/kirjasto

ISBN: 978-952-61-2478-0 (print)
ISSNL: 1798-5668
ISSN: 1798-5668
ISBN: 978-952-61-2479-7 (pdf)
ISSNL: 1798-5668
ISSN: 1798-5676

Author's address:
University of Eastern Finland
Department of Applied Physics
P.O. Box 1627
70211 Kuopio
Finland
email: paavo.vartiainen@uef.fi

Supervisors:
Professor Pasi A. Karjalainen, Ph.D.
University of Eastern Finland
Department of Applied Physics
Kuopio, Finland
email: pasi.karjalainen@uef.fi

Professor Jari Arokoski, M.D.,Ph.D.
University of Helsinki and Helsinki University Hospital
Department of Physical and Rehabilitation Medicine
email: jari.arokoski@hus.fi

Reviewers:
Professor Aki Mikkola, D.Sc. (Tech)
Lappeenranta University of Technology
Department of Mechanical Engineering
email: aki.mikkola@lut.fi

Professor Janne Avela, Ph.D.
University of Jyväskylä
Neuromuscular Research Center
Faculty of Sport and Health Sciences
email: janne.avela@jyu.fi

Opponent:
Professor Jari Hyttinen, Ph.D.
Tampere University of Technology
Faculty of Biomedical Sciences and Engineering
email: jari.hyttinen@tut.fi

Paavo Vartiainen
Advanced methods for human motion analysis - applications to gait and spine biomechanics
Kuopio: University of Eastern Finland, 2017
Publications of the University of Eastern Finland
Dissertations in Forestry and Natural Sciences

ABSTRACT

Human motion analysis can be defined as the systematic study of human motion by visual inspection and quantitative observations. This thesis focuses on quantitative measurements of human gait and back motion.

In publication **I**, kinematic and kinetic changes in obese gait following bariatric surgery were examined. The study revealed that hip and knee moments are reduced in proportion to the amount of weight lost and that step width becomes reduced. The challenges in data analysis encountered in this study stimulated the development of advanced methods suitable for this kind of analysis.

In publication **II**, a novel method was developed for the estimation of human kinematics, based on state-space modeling. The state consists of the positions, orientations, velocities, and accelerations of an articulated 3D model. The estimation is performed using the unscented Kalman filter (UKF) algorithm with a fixed-interval smoother. Impulsive acceleration at floor contact of the foot is estimated by implementing a contact constraint in the UKF evolution model. The constraint inserts an acceleration impulse into the model state.

The estimation method was applied to marker-based motion analysis in a motion laboratory. Validation measurements were performed with a rigid test device and with human gait. A triaxial accelerometer was used to evaluate the estimates of acceleration. Comparison between the proposed method and the extended Kalman smoother showed a clear difference in the quality of estimates during impulsive accelerations.

The proposed approach enabled estimation of human kinematics during both continuous and transient accelerations. The approach provided a novel way of estimating acceleration at foot initial contact, and thus enables more accurate evaluation of loading from the beginning of the floor contact.

In addition to acceleration estimation, method developed in study **II** has benefits in processing data from multiple cameras. Unidentified marker observations from each camera can be used as input data for the UKF algorithm. The articulated 3D model and UKF predict-step are utilized is online identification of marker observations.

In publication **III**, a novel method to estimate the 3D shape of the spine during motion was proposed. The method involves several steps i.e. a measurement setup, a model of whole spine and data processing methods based on quaternion algebra. The measurement setup consisted of inertial sensors mounted on the skin of the back. The model incorporates 3D segments, articulated together and it includes every vertebra of the spine and segments of lower body. The locations of the sensors with respect to vertebrae are incorporated into the model. The accuracy of the model was evaluated against camera-based motion capture. Furthermore, the angles between the vertebrae in three anatomical planes were examined. Measurements showed that the proposed method can be used to measure spinal shape in the sagittal plane during motion. The shape measurement can be utilized in real-time measurement and analysis of spinal postures during everyday activities, such as lifting tasks.

In addition, in this thesis novel technologies for motion capture are reviewed. There are two main categories of novel methods i.e. wearable sensors, such as inertial sensors in study **III** and methods utilizing modern camera technologies. Most of the novel methods provide the possibility of a low-cost and easy-to-use motion capture for animation purposes. The capabilities of these methods for accurate motion analysis are examined based on recent publications. The novel methods appear to be feasible alternatives for conventional marker-based motion analysis, at least in some applications.

National Library of Medicine Classification: QT 34.5, WE 103, WE 725, WE 860, WE 870

Medical Subject Headings: Biomechanical Phenomena; Motion; Movement; Gait; Walking; Hip Joint; Knee Joint; Obesity; Overweight; Weight Loss; Bariatric Surgery; Algorithms; Acceleration; Spine; Models; Biological; Humans

TIIVISTELMÄ

Ihmisen liikkeiden mittaaminen ja mittaustiedon analysointi, liikeanalyysi, tarjoaa tietoa asennoista, liikeradoista sekä kuormituksista arkipäivän liikkeiden aikana. Tässä väitöskirjassa tarkastellaan keskeisiä liikeanalyysin menetelmiä. Väitöskirjan osajulkaisuissa sovellettiin ja kehitettiin edistyneitä menetelmiä kävelyn aikaisen nivelkuormituksen määrittämiseen sekä selän muodon tarkasteluun liikkeen aikana.

Ensimmäisessä osatyössä analysoitiin kävelyn muutoksia nopean painonpudotuksen yhteydessä. Tutkittavat potilaat (N=13) olivat ylipainoisia, joille suoritettiin laihdutusleikkaus. Mittaukset suoritettiin monen kameran järjestelmää käyttäen ennen ja jälkeen painonpudotuksen. Painonpudotuksen vaikutusta kävelyn etenemiseen tarkasteltiin määrittämällä ensiksi kinemaattisia parametreja, kuten askelpituus, -leveys, -nopeus ja nivelkulmat. Lisäksi estimoitiin polvi- ja lonkkaniveliin kohdistuvat vääntömomentit määritetyn kinematiikan ja voimalevymittausten perusteella. Nämä vääntömomentit kuvaavat nivelpintoihin kohdistuvaa kuormitusta kävelyn aikana. Tässä tutkimuksessa tarkasteltiin erityisesti kuormitusmuutoksia suhteessa kehonpainon muutokseen. Valtaosin polvi- ja lonkkavääntömomentit pienenivät samassa suhteessa kuin paino putosi. Kävelyn kinematiikassa merkittävin ero oli askelleveyden kapeneminen. Tämän osatyön dataa käsiteltäessä havaittiin virhelähteitä, jotka voivat heikentää määritettyjen parametrien tarkkuutta.

Ensimmäisessä osatyössä havaittujen virhelähteiden vuoksi toisessa osatyössä kehitettiin kamerapohjaisen liikeanalyysiin menetelmää, jota käyttäen kappaleen kolmiulotteinen liike, nopeus ja kiihtyvyys määritetään. Menetelmässä käytetään havaintoina kameroilta saatavia kaksiulotteisia pisteitä. Menetelmässä määritellään geometrinen malli, jonka liiketilaa estimoidaan Kalman suodin-algoritmilla. Tämä mallipohjainen menetelmä toimii aiempia menetelmiä tarkemmin, kun havainnoissa on puuttuvia tai virheellisiä pisteitä. Algoritmissä käytettiin lisäksi nk. unscented-muunnosta. Unscented-muunnos mahdollistaa epälineaaristen funktioiden käytön Kalman suotimen tilafunktiona ja havaintomallina. Epälineaarisen tilafunktion käyttö mahdollistaa kiihtyvyyspiikkien aiempaa tarkemman estimoinnin liikelaboratorion mittauksissa. Kalman suotimen lisäksi toteutettiin nk. Kalman smoother – algoritmi, joka parantaa menetelmän tarkkuutta poistamalla viivettä nopeus- ja kiihtyvyysestimaateista.

Kolmannessa osatyössä kehitettiin mittausjärjestely, ohjelmisto ja matemaattiset menetelmät selkärangan kolmiulotteisen asennon määrittämiseksi liikkeen aikana. Mittauksessa käytettiin langattomia inertia-antureita, jotka kiinnitettiin ihon pinnalle. Selkärangan asennon määrittämiseksi muodostettiin kvaternioalgebraa hyödyntäen malli, jolla jokaisen nikaman asentoa voidaan tarkastella.

Kolmannessa osatyössä käytetyt inertia-anturit ovat hyvä esimerkki siitä, kuinka uusia teknologisia ratkaisuja voidaan hyödyntää liikeanalyysissä. Inertia-anturien lisäksi uusia kamerateknologioita käytetään liikkeen mittaamiseen, erityisesti elokuva- ja peliteollisuudessa. Tässä väitöskirjassa tarkastellaan tuoreiden julkaisujen perusteella, kuinka näitä laitteita voidaan käyttää liikeanalyysin mittauksissa ja kuntoutussovelluksissa.

Yleinen suomalainen asiasanasto: biomekaniikka; liikeanalyysi; kävely; lantio; polvet; lihavuus; ylipaino; kiihtyvyys; selkäranka; 3D-mallinnus; algoritmit; mittausmenetelmät; matemaattiset menetelmät; estimointi; mallintaminen; matemaattiset mallit; bayesilainen menetelmä; ihminen

ACKNOWLEDGEMENTS

This study was carried out during the years 2011-2017 in the Department of Applied Physics at the University of Eastern Finland.

First and foremost, I would like to thank my supervisors and coworkers; Professor Pasi Karjalainen, Ph.D. and Docent Jari Arokoski, M.D, Ph.D. My most important co-worker during the studies of the thesis was Mr. Timo Bragge.

I also want to thank all emeritus and present members of the Biosignal analysis and Medical Imaging (BSAMIG) research group, and in fact all the people with whom I have worked with during these years.

Second, I wish also to thank the reviewers Prof. Aki Mikkola and Prof. Janne Avela. They both gave useful comments and specific suggestions, which helped me to finalize the text.

I want to acknowledge my financial supporters, the strategic funding of University of Eastern Finland, the International Doctoral Programme in Biomedical Engineering and Medical physics (iBioMEP), Kuopio University Hospital (EVO, grant 5960431) and Instrumentarium Science Foundation.

Finally, I wish to thank all the people in my extracurricular life. I have been privileged to have close relationships with several family members throughout my life.

UNIVERSITY OF
EASTERN FINLAND

Kuopio, April 2017

Paavo Vartiainen

LIST OF PUBLICATIONS

This thesis is based on the following original publications:

I Vartiainen P., Bragge T., Lyytinen T., Hakkarainen M., Karjalainen P.A., Arokoski J.P.A., “Kinematic and kinetic changes in obese gait in bariatric surgery-induced weight loss”. *Journal of Biomechanics.* Jun 26;45(10): 1769–1774; doi: 10.1016/j.jbiomech.2012.05.002 (2012).

II Vartiainen P., Bragge T., Arokoski J.P.A., Karjalainen P.A., “Nonlinear state-space modeling of human motion using 2-D marker observations”. *IEEE Transactions on Biomedical Engineering.* 61(7):2167–2178; doi: 10.1109/TBME.2014.2318354 (2014).

III Vartiainen P., Bragge T., Karjalainen P.A., “Measurement and modeling of spinal shape using inertial sensors - comparison to camera-based motion capture”. Submitted to Journal of Medical and Biological Engineering.

AUTHOR’S CONTRIBUTION

In study **I**, the author participated in the developed of the measurement facilities and in gathering the measurement data. The author analyzed the measurement data. The senior author of the publication, Dr. Jari Arokoski, made a major contribution to publication **I**. His experience on clinical studies stimulated a comprehensive discussion about the results.

The hypothesis for study **II** was generated from the previous work of the author and in discussions with Mr. Timo Bragge in the field of motion analysis. The author implemented the algorithms presented in publication **II**.

Study **III** involved putting new measurement equipment into operation. The author planned the measurements and applied for the ethical approvals of the study. The author programmed applications for data collection and analysis. The author carried out several pilot measurements and recruited volunteers for the measurements.

The author was the main writer of all three publications. The author prepared the figures and tables of the publications. The author utilized various features of MATLAB software environment in implementing algorithms, data processing applications, graphical user interfaces and figures.

Contents

1 Introduction

Human motion analysis can be defined as the systematic study of human body motion by visual inspection and measurements. Motion analysis can provide information on an individual's movements during everyday life. In addition to the actual motion itself, also the forces affecting skeletal structures are of interest. External forces that arise from gravity and the internal forces produced by the muscles both contribute to the motion and forces. Forces on the knee and hip joints and at the lower back are widely used to assess loading during motion.

Various measurement devices are used in motion analysis e.g. cameras, force sensors and devices for measuring angles. Some of the devices, such as multiple camera systems and force platforms require a dedicated laboratory. Wearable devices, which measure angles and orientations, do not need to be used only in a laboratory. Practically all devices in motion analysis are non-invasive and the methods do not cause any radiation exposure. At their best, measurements of motion can be done while the subject is undertaking everyday activities. For example, walking is a common everyday activity and thus gait analyses are widely carried out in motion research.

This thesis focuses on two widely used methods in human motion analysis. The so-called marker-based method [1] requires a multiple camera system. Reflective markers are mounted on the skin and the positions of the markers during motion are reconstructed using the camera system. This marker-based method can be considered as the gold standard human motion capture technique. A marker-based motion capture was utilized in study **I**. In study **II**, an advanced method based on the marker-based measurement was developed. In study **III** so-called inertial sensors were applied to devise a method which could model spine shape during motion.

In addition, novel technologies for motion capture are reviewed in this thesis. Recent advances in inertial sensor technology have led to the development of wearable motion capture systems. An other category of novel methods is based on modern machine vision technologies, such as structured light and time-of-flight cameras. These methods are primarily intended to provide easy-to-use motion capture for animation purposes. The suitability of these technologies for motion analysis is reviewed based on recent publications. The benefits and limitations of the methods developed in studies **II-III** and methods based on novel technologies will be discussed.

2 Background

2.1 GAIT ANALYSIS - KINEMATIC ANALYSIS AND JOINT MOMENTS

A common procedure for measuring walking patterns in the laboratory is called gait analysis. Gait analysis can be used to quantify gait deviations [2]; common applications include stroke rehabilitation monitoring [3], evaluation of treatment efficacy in Parkinsons' disease [4] and assessment of changes associated with aging [5]. Musculoskeletal conditions, such as knee [6,7] and hip osteoarthritis [8] are central application areas for gait analysis.

By using a multiple camera system three-dimensional kinematics during gait can be captured. Gait kinematics is examined in three anatomical planes. Figure 2.1 illustrates the terminology used for the hip, knee and ankle angles in the sagittal and frontal planes. Axial rotations of the body segments occur in the transverse plane. One critical issue in gait analysis is the definition of the zero level of angles [9]. Due to different zero level definitions between studies [10], it is recommended to report changes in angle values rather than absolute values.

Once the kinematics of feet, legs, thighs and pelvis are reconstructed, various parameters can be calculated. Parameters describing the duration and geometry of gait cycle are called spatio-temporal parameters or cadence parameters. Commonly reported cadence parameters include walking speed, step length and step width. Kinematic parameters, such as ankle, knee and hip joint angles are used to quantify differences in walking style. Kinetic parameters, i.e., forces and moments, provide estimates of the loadings on the joints. Examples of hip, knee and ankle joint angles and moments during a gait cycle are illustrated in Fig. 2.2.

Force platforms, which measure magnitude, direction and application point of ground reaction force are needed for calculating kinetic parameters. The so called external joint moment arises from the position of the joint with respect to the ground reaction force vector during motion. The internal moment is generated to balance external moment. Internal and external moments are exactly the same only when the angular acceleration of the joint equals zero. However, the contribution of the angular accelerations to the joint moment during stance phase are very small. Especially in the frontal plane, angular acceleration is negligible. Therefore, it is acceptable to compare frontal plane moments reported in different studies, whether the reported "KAM" is internal knee abductor moment or external knee adduction moment. In the publication **I**, internal moments are reported.

Knee joint moments have gained an established role in describing knee loading. In particular, the knee adduction moment describes loading at the medial compartment of the knee [11]. Thus, the knee adduction moment has become a standard parameter in knee osteoarthritis studies [12, 13]. The magnitude of the knee adduction moment has been shown to be associated with medial knee osteoarthritis [14]. An increase in the knee adduction moment is mainly due to a varus malalignment of the knee [15, 16]. Knee orthoses, which fix varus malalignment, are meant to reduce knee adduction moments. Another way to fix malalignment is a surgical procedure called tibial osteotomy. Effects of knee orthoses and osteotomy can be assessed analyzing knee adduction moments during gait.

The sensitivity analysis conducted by Ardestani et al. [17] revealed in detail how modifications in joint kinematics change joint moment values. Ardestani et al. used principal component analysis to quantify the causal relationships. This analysis is useful when trying to find the best gait modifications that can reduce joint loadings.

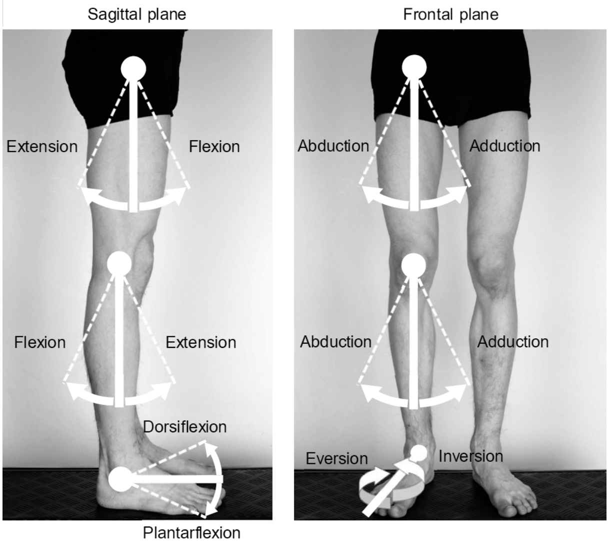

Figure 2.1: Nomenclature of the angles of lower limb joints in two anatomical planes [18]. Axial rotations of the joints occur in transverse plane.

2.1.1 Impacts of obesity and weight loss on gait

There are inconsistent reports of the kinematic and kinetic parameters of walking in obese but otherwise healthy subjects. Several studies claim that obese adults or children have a shorter step length, a wider step width and a longer double support time [19–22] and [23]. Furthermore, peak knee flexion angles during the stance phase have been reported as being lower [24, 25] and a smaller range of knee and hip motion in obese people has been described [26]. However, there are studies where no differences in cadence, stride length or double support time have been detected between obese and healthy weight children [27], and knee flexion angles have also been found to be identical in some studies [19, 22]. Devita et al. [25] stated that obese but otherwise healthy subjects had less absolute sagittal plane knee moment at their self-selected walking speed but an equal moment while walking at the same speed as lean individuals.

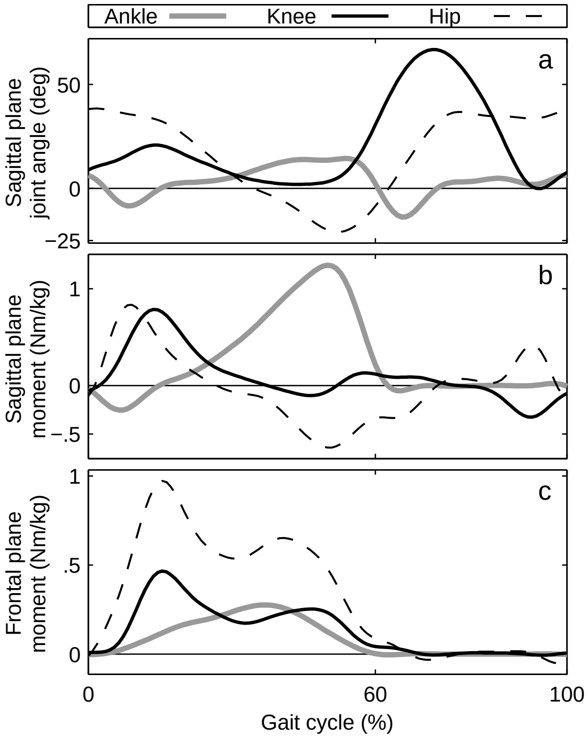

Figure 2.2: (a) Sagittal plane angles of ankle, knee, and hip joints over a normal gait cycle. Flexion and dorsiflexion angles are positive. (b) Sagittal plane joint moments normalized by body weight, extensor and plantar flexor moments are positive. (c) Frontal plane normalized moments, abductor moments (i.e. external adduction moments) are positive

The first study evaluating the effects of bariatric surgery-induced weight loss on gait of obese individuals was published by Hortobagyi et al. [28]. The subjects of the study were obese but otherwise healthy, the average weight loss was 33.6% (42.2 kg). Weight loss increased swing time and stride length at both the self-selected and the standard speed. Weight loss also increased the self-selected speed. At the self-selected speed, the normalized peak knee extensor moment increased whereas the absolute ankle and frontal plane knee moments declined after weight loss. At a fixed speed, no significant change was observed in normalized hip, knee or ankle moments.

The effects of weight loss on joint loading in obese knee OA patients has been examined in two studies [29, 30]. Messier et al. [29] showed that each one-kilogram reduction in body weight was associated with a 1.4% reduction in peak knee abductor moment after statistically adjusting for several variables including age, walking speed, gender and subjective scores on knee pain and function. The average weight loss in their study was only 2.6%. The subjects in the study of Aaboe et al. experienced greater weight loss; the average reduction in body mass was 13.5% [30]. They observed a significant reduction of up to 13% in peak knee abductor moment but no significant changes in sagittal plane knee moment at the participants' freely chosen walking speed.

A more extensive review on the impacts of obesity and weight loss on gait was conducted by Lyytinen et al. [31]. As bariatric surgery is increasingly being utilized along with other obesity treatments, several biomechanical studies on the effects of intensive weight loss have been conducted recently [32–35]. In addition to Lyytinen et al., two review articles focusing on bariatric surgery-induced gait changes have been published [36, 37].

In most of the gait studies, the interval between the baseline and follow-up measurements has been less than one year [28, 38]. Long-term gait changes were examined by Froehle et al. [32] who performed follow-up measurements at 4 to 5 years the after bariatric surgery. They observed an increase in step length, gait speed and cadence after the weight loss. Similarly to the findings in study **I**, step width was decreased and in addition, there was a decrease in double support time.

2.2 MARKER-BASED MOTION ANALYSIS

The basic method to utilize 2D coordinates of the markers observed by cameras involves the reconstruction of the 3D coordinate of each marker at every time step. Then, these 3D points are used to determine the position and orientation of the body parts. Thus, the geometry of the body parts is obtained directly from the reconstructed points at each time step. This method leads to erroneous geometry, if data has missing or misidentified points. During gait, the number of cameras seeing a marker varies due to occlusions caused by the opposite leg. If only one camera sees a marker, the 3D point cannot be reconstructed. Misidentifications may occur when two markers diverge after overlapping in a camera image. When a misidentification occurs, the resulting 3D point may contain a large error.

The markers placed on the skin or cloth have certain errors initially and the markers also move with respect to the underlying bones during the motion. The motion of the markers with respect to the underlying skeletal structures, the so-called soft tissue artefact (STA), is a major error source. Several studies have attempted to quantify the magnitude of the STA and to suppress its influences [39–43]. For example, fluoroscopy has been used to quantify STA [44, 45]. It is widely recognized that accurate measurement of axial rotations of knee requires fluoroscopy [45, 46].

To overcome the problems with missing and misidentified observation and the STA, a wide variety of model-based methods have been developed [47, 48]. In these methods, a geometrical model is defined in 3D space. These models typically have fixed dimensions and the segments are articulated together. The model corresponds to the body parts of the person who had the markers on his/her skin during the measurement.

One of the mathematical methods used for fitting the model to the observations is Kalman filtering. Kalman filter and its extensions extended Kalman filter and unscented Kalman filter are algorithms that can estimate the pose of the model using the data available from the whole measurement [49]. By combining state estimation with a geometrical model, the position and orientation of the model segments are estimated throughout the motion. In addition, the linear and angular velocities and accelerations of the model segments are incorporated in the estimation. The set of parameters that determine poses, velocities, and accelerations of model segments constitutes a kinematic state. This time-varying state can then be estimated by the Kalman filter [50].

The Kalman filter is based on a state evolution model and an observation model [51]. At every time step, the state evolution model receives the previous state estimate as an input and makes a prediction of the state. After this, the observation model is used to update the prediction based on observations of the time step. The filter can estimate a state that is not observed directly, since the observation model maps the state to the observable space. Mappings from 3D space to camera image planes can be included in the observation model; this involves utilizing observations on the image planes at the current time instant [52]. Parameters of the Kalman filter determine how quickly values of the estimates can change, and how the observations will be weighted in estimation. An additional improvement to the algorithm is fixed-interval Kalman smoother [53, 54], which uses data from the whole measurement in the estimation.

The state evolution model of Kalman filter predicts how the motion progresses from the previous time step to the current time. State evolution models, which assume that the motion will continue smoothly are commonly used in human motion tracking [52, 55]. If the actual motion has a rapid change, this kind of model cannot make a reasonable prediction.

In the method proposed in study **II**, the estimation of the rapid changes was improved by changing the state evolution model. In the measurements of study **II**, the state evolution model was changed, when a floor contact was detected.

Furthermore, mappings from 3D space to camera image planes are included in the observation model in study **II**, thus 3D reconstructions are not necessary. This enables the utilization of those observations, which are seen only by a single camera. In addition, the observations which are viewed by more than two cameras are given greater weight in the estimation. This feature improves the accuracy, if all the cameras are calibrated with adequate accuracy. The observation model of the algorithm can be modified depending on the available data, one possibility is to use reconstructed 3D points.

Dimensions of a geometrical model, eg. segment lengths and joint points are typically fixed based on calibration measurements. The accuracy of the knee and hip joint points affect the values of the kinematic and kinetic parameters. So-called functional methods, where the center points are determined based on dynamic calibration measurements have been developed [56, 57]. Functional methods have also been utilized in defining the joint axis of knee [58] and ankle joint [59].

Mappings from 3D space to camera image planes are defined during the calibration of cameras. The camera calibration algorithm was implemented according to Hartley and Zimmerman [60]. Nonlinearities of camera optics are taken into account by modeling radial and tangential distortions of the optics using four parameters [61].

2.3 CHALLENGES IN SPINE MOTION ANALYSIS

Posture and motion of the vertebral column during daily activities are important when assessing loading and risk of injury. However, the possibilities to reliably measure the spinal motion during everyday activities, such as occupational tasks have been limited. Camera-based systems can be used to capture motion of the back surface, but estimating the spinal kinematics has proved to be a challenging problem even in the laboratory environment [62, 63].

The geometry of lumbar and thoracic spine during forward bending is inherently complicated due to natural curvature of the spine in the standing posture. During forward bending, the spine first straightens and bends forwards at the end of the movement. Since there are several layers of muscle and fat tissue between vertebrae and skin, the estimation of vertebral postures is challenging [42, 64].

There are no practical methods for measuring orientations of individual vertebrae during motion. Imaging methods, such as X-ray and MRI, which show contours of the vertebrae, provide the fundamental basis for the estimation of the orientations. However, this kind of imaging reveals only one static posture at a time. Motion estimation demands that one captures images at different postures. Taking several X-ray images increases radiation exposure. MRI-imaging in natural postures requires the availability of the so-called open upright scanner [64].

Imaging methods typically provide two-dimensional outlines of the vertebrae, thus three-dimensional (3D) orientations of the vertebrae cannot be observed. The 3D orientations can be estimated using skin-mounted sensors, which measure their own orientation. These 3D orientations can be used to estimate the so-called coupled motions of the spine [65–67]. The coupled motions mean the motions occurring in directions other than the primary motion [68]. Spinal motion is commonly analyzed in three anatomical planes. Forward-backward bending occurs in the sagittal plane, left-right bending in the frontal plane and spine rotation in the transverse plane. Forward bending corresponds to flexion of the spine and backward bending corresponds extension. Left-right bending is normally abbreviated to lateral bending. Chhikara et al. [69] measured lateral bending of lumbar spine. These workers used two inertial sensors and reflective markers mounted on the sensors to compare accuracy with camera-based motion capture. They reported that there was a good agreement in the angle values between camera-based and inertial measurement, with RMS with the errors being below three degrees.

Other methods previously used to estimate the shape of the spine include strain gauge strips [70] and profilometers [71]. One commercially available device is SpinalMouse [72], which can be used to estimate the spinal shape in static postures.

Yang et al. [73] studied angular and translational motion of the lumbar vertebrae of osteoporotic patients. They used X-ray-images and skin-mounted sensors (Fastrak®). Their setup enabled only two-dimensional analysis of forward bending, i.e., flexion-extension motion. They concluded that skin-mounted sensors could estimate the angular motion between the vertebrae with acceptable accuracy, whereas the translational motions could not be estimated reliably. In their later study, Yang et al. [74] analyzed the error of skin-mounted sensors and found that a sensor located on sacrum suffered from a greater error than a sensor on L1 vertebra. They also observed that skin sliding and sensor tilting with respect to vertebrae typically introduced errors in opposite directions.

Inertial sensors, consisting of gyroscopes, magnetometers and accelerometers, have been used in a wide variety of applications, thanks to their portability and ease of use [75, 76]. The sensors provide continuous orientation data in real time. The earlier inertial sensor applications developed for the spine motion estimation consisted of two [77,78], three [79] or four [80] sensors, and only sagittal plane motion was examined in reports [79] and [80].

The measurement setup in the study **III** consists of seven wireless sensors along the spine, thus the 3D spinal shape can be estimated in more detail. Sensors used in this study are commercially available from Xsens Technologies. The high technical accuracy of the sensors has been reported earlier [81, 82].

Similarly to the gait analysis, inverse dynamics can be used to assess loading of the spine. One commonly determined parameter is the moment in the joint between

L5 and L4 vertebrae [83]. A standard inverse dynamics procedure has been used to calculate the moment at the L5/L4 joint. Commonly L5 vertebra is fixed to the pelvis segment.

2.4 RECENT DEVELOPMENTS IN MOTION CAPTURE AND THEIR APPLICABILITY TO QUANTITATIVE ANALYSIS

2.4.1 Markerless camera technologies

The marker-based method presented in section 2.2 requires mounting of reflective markers on specific locations on the skin. Therefore, several methods which do not require markers have been proposed [84, 85].

Using a suitable camera system and algorithms, the silhouette of the 3D object can be estimated. The so called visual hull concept [86, 87] is widely used in these markerless methods. Ceseracciu et al. [88] proposed a method for comparison of marker-based and visual hull -based motion capture through simultaneous measurements. They did not obtain reasonably accurate values for joint angles during gait. Visual hull-based methods are not reliable in tracking the axial rotations of the body segments or orientations of feet segments [89]. Recently, Perrot et al. [90] proposed visual-hull based method for joint angle measurement; they concluded that the range of knee and hip joint motion matched the value obtained with the marker-based method.

Structured light and time-of-flight (ToF) [91] are machine vision technologies where distance of every pixel from a camera is determined. Recently, these techniques have been applied in motion capture and gait analysis [92]. The best known and most affordable devices based on the techniques are the two versions of Microsoft Kinect. They were released to provide motion capture for Xbox games. The first version of Kinect was based on structured light. The device has IR laser projector, which projects a know pattern of IR light. An IR camera of the device detects the pattern, as it reflects back from the scene. Depth map of the scene is infered from the deformation of the IR pattern [93].

Kinect is designed to capture the human figure, when a person is facing towards the camera. Thus, studies evaluating the suitability of Kinect V1 for frontal plane motion analysis have been conducted [94]. Huber et al. studied the feasibility of Kinect in shoulder joint angle tracking [95]. They observed that the test-retest reliability of shoulder angle was good, except for the flexion movement where the shoulder joint was occluded from the Kinect by the arm. Moreover, the discrepancies between Kinect and goniometer were clinically significant in all shoulder poses. Thus, accuracy of sagittal plane joint angles is limited [96]. Therefore, when Kinect is utilized in gait analysis, a custom measurement setup and data processing is required [97]. For example, Pfister et al. [98] placed Kinect at a 45 angle with respect to the walking direction. The spatio-temporal parameters such as gait speed and step time have shown acceptable accuracy and repeatability [37]. The accuracy of Kinect during treadmill walking was evaluated by Xu et al. [99]. In their setup, Kinect was located in front of the treadmill. Tracking of ankle joint position was not reliable with this setup, and thus step width was not accurately detected.

Kinect V2 was released in 2015; the new version is based on ToF technology. Xu et al. compared joint center location estimation with Kinect V1 and with V2 [100]. They found no significant differences in the accuracy of the estimation between the two versions. Clark stated that Kinect V2 was only moderately accurate for measuring medial-lateral motion, significant bias was observed in concurrent measurements with the camera system [101]. Kuster et al. [102] examined the accuracy of the Kinect V2 in quantifying upper body motions. They stated that it had sufficient accuracy except in those motions where the arm occluded the shoulder joint, similarly to Huber's observations with Kinect V1. Kuster et al. also noted that bias compared to camera-based system was smaller in the seated position. One factor affecting the accuracy is the vertical positioning of the Kinect camera, which was placed 1.2 m above the floor in their study.

Geerse et al. [103] proposed utilizing four Kinects to capture several steps in over-ground walking. The limited accuracy of step width was also found in over-ground walking [103]. They achieved good agreement in a 3D point time series when they compared Kinect and a camera system. Mentiplay et al. [104] used a single Kinect V2 for gait analysis. They were not able to accurately assess lower body kinematics during gait.

Joint location estimation with the Kinect is based on the scanned surface. Thus, individual size and shape of muscles and adipose tissue makes Kinect unsuitable for several clinical applications, including obesity and weight loss studies. In addition, clothing and bulky measurement equipment on the subject may affect the estimated joint locations.

Recently, Eltoukhy et al. [105] compared Kinect with a camera-based system in treadmill walking. They placed the Kinect camera in front of the treadmill; their results indicated that Kinects had acceptable accuracy in hip and knee joint angles, but poor accuracy for assessing the ankle joint angle. They noted that Kinect underestimated step length and width compared to the camera-based system.

Several measurement setups of multiple Kinects have been used to capture three-dimensional motion. Recently Yang et al. proposed a solution using three Kinect cameras [106], they conducted their measurement with the subject walking three meters in a straight line. The Kinect-based system for recording several consecutive steps are not straightforward to implement. Another limitation of Kinect is its fixed sampling rate, it provides orientation data at 30 Hz. Nonetheless, the Kinect camera is able to capture IR images at 300 Hz and one method for tracking motion at 300 Hz using raw data of Kinect has been proposed [107].

Several Kinect-based applications for elderly care and stroke rehabilitation have been proposed [108]. These applications include fall detection [109] and exercise games [110].

The same structured light technology used in Kinect V1, is used in Intel® RealSense™cameras [111]. The cameras can be used with a laptop to capture gestures of hands and facial expressions of the user. Several models of RealSense cameras are available, and also a software development kit is provided [112]. Thus RealSense cameras can be used in developing various human-computer interaction applications [113].

2.4.2 Inertial sensor applications

Wireless inertial sensors offer a feasible way to capture whole body kinematics outside the laboratory, only a wireless connection to a laptop is needed to record data. Thus, inertial sensors have been used in workplace ergonomic assessments [114–116]. The sensors have also been utilized in several sports applications, such as alpine skiing [117] and snow-boarding [118], ski-jumping [119, 120] and swimming [121]. Novel methods that improve joint angle estimation during inertial sensor measurement [122, 123], and methods that estimate joint moments using only inertial sensors [124] ,ay be advantageous in further development of inertial sensor-based methods.

If a novel inertial sensor-based is intended to replace conventional marker-based analysis in the motion laboratory, the method must be compared with the conventional method in concurrent measurements. In publication **III**, this kind of comparison was conducted in an application evaluating back motion. With respect to clinical gait analysis, only a few comparative studies have been made [125, 126].

An inertial sensor can capture the whole body motion ambulatory. In contrast, ground reaction forces (GRFs) cannot be measured outside the laboratory. Therefore, several methods to estimate GRF without force platforms have been proposed [124, 127, 128]. Ren et al. [127] described a method based only on camera-based motion capture. The major problem in camera-based methods is the difficulty in estimating how the total GRF is divided between the two feet. Sim et al. [128] proposed a method using pressure insoles; their method exploits a wavelet neural network.

3 Aims

Specific aims of the original publications are as follows.

1. To quantify the kinematic and kinetic changes associated with bariatric surgery-induced weight loss in obese subjects using a model-based method.
2. To develop a state-space estimation method, which accurately determines position, orientation and acceleration of human body segments based on 2D marker observations during both smooth and rapidly changing motion.
3. To devise a novel method to estimate 3D shape of the spine during motion. This method incorporates inertial sensor measurements, geometrically realistic model of whole spine and data processing methods based on quaternion algebra.

4 Materials and methods

In this section, first the the measurement laboratory used in the study is introduced. Furthermore, mathematical concepts for presenting three-dimensional orientations are described. Subsequently, the methods utilized and developed in studies **I-III** are presented.

4.1 MOTION LABORATORY

The measurements of the present study were carried out in the motion laboratory of the Department of Applied Physics, University of Eastern Finland. The laboratory has been planned and built for clinical gait analysis [129–131]. The laboratory equipment consists of high-speed cameras with an in-house developed camera data acquisition system and a walkway with two embedded force platforms (Model OR6-7MA, AMTI Inc., MA, USA). Different measurement devices, such as an EMG measurement system and pressure insole systems, can be synchronized with the camera system using photo cells, and radio frequency triggers. Figure 4.1 illustrates the data collected in motion laboratory.

The camera system consists of six high-speed Firewire (IEEE 1394) cameras (model Basler A602f) for motion capture. The resolution of the cameras is 656×491 pixels; the frame rate used in studies **I-III** was 100 frames/s. The cameras are equipped with IR illumination LEDs and IR filters. Reflective, spherical markers are attached on the subject. In studies **I** and **II** markers of diameter 18 mm were used, they were mounted on the skin and spandex suit. Only the markers should be visible to cameras, other materials in the laboratory are selected so that they do not reflect IR light. Raw images from the cameras are saved as 8-bit grayscale images. Pixel coordinates of the centroids of the markers are detected from these images using an in-house developed algorithm, implemented in NI LabVIEW 2010. Laboratory has a walkway, where subject has space to take several steps before the two force platforms.

In study **II**, a triaxial piezoresistive accelerometer (Meac-x®, Mega Electronics Ltd, Kuopio, Finland) was used in addition to the camera system. The range of the accelerometers is ± 10 g, the resolution is 0.0015 g and the sampling rate 1000 Hz. The accelerometer data were collected using Biomonitor ME6000® telemetric datalogger (Mega Electronics Ltd). The datalogger was synchronized with the camera system using a radio frequency trigger.

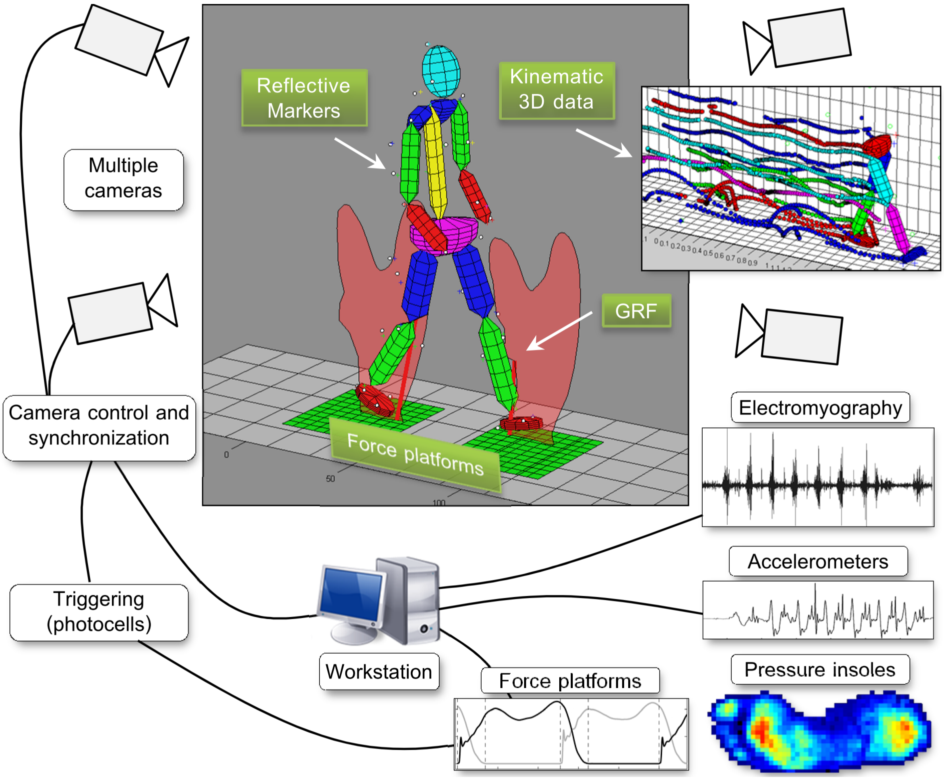

Figure 4.1: Measurement devices in the motion laboratory. The camera system and force platforms are synchronized using photocells. Additionally, accelerometers, electromyography and pressure insoles can be added to the synchronized measurement.

4.2 PRESENTATION OF 3D ORIENTATIONS

One fundamental aspect of motion analysis involves the possibility to create mathematical representation of 3D orientations. Orientations of moving objects and transformations between coordinate systems have to be handled robustly during the measurement and analysis.

Quaternions are an extension of complex numbers and they have their own algebra [132]. A quaternion is given $q = \left[q_{(1)} + q_{(2)}\mathrm{i} + q_{(3)}\mathrm{j} + q_{(4)}\mathrm{k}\right]$, where $q_{(1)}$, $q_{(2)}$, $q_{(3)}$ and $q_{(4)}$ are real numbers. Imaginary part of the quaternion has three components, the definition includes three different imaginary units i, j and k.

A practical convention is to denote quaternion as a vector q, $q \in \mathbb{R}^4$:

$$q = \begin{bmatrix} w \\ \vec{v}_q \end{bmatrix}, \tag{4.1}$$

where $w \in \mathbb{R}$ is the real part, $\vec{v}_q \in \mathbb{R}^3$ is the imaginary part.

Quaternions, whose norm equals one are called unit quaternions. The unit quaternions are commonly used for 3D orientation representation, especially in computer graphics [133]. They provide robust, singular-free method for representing arbitrary rotations in 3D space. A unit quaternion q_1 can be used to represent an orientation in a reference coordinate system or a rotation between two orientations. Consecutive rotations are represented using quaternion multiplications. Rotation q_2 followed by rotation q_1 is a quaternion multiplication

$$q_1 q_2 = \begin{bmatrix} w_1 w_2 - \vec{v}_{q1} \cdot \vec{v}_{q2} \\ w_2 \vec{v}_{q1} + w_1 \vec{v}_{q2} + \vec{v}_{q1} \times \vec{v}_{q2} \end{bmatrix} \in \mathbb{R}^4, \tag{4.2}$$

where $\cdot$ is a scalar product and $\times$ is a vector product.

The conjugate of a unit quaternion represents the inverse rotation of the rotation designated by q, defined as

$$q^* = \begin{bmatrix} w \\ -\vec{v}_q \end{bmatrix}. \tag{4.3}$$

The orientation q_2 with respect to orientation q_1 is expressed by the relative quaternion q_{rel},

$$q_{\text{rel}} = q_1^* q_2. \tag{4.4}$$

The orientation q_{rel} is in coordinate system spanned by q_1.

Even though unit quaternions have four components, they have only three degrees of freedom, due to the normalization. Thus, the components of a unit quaternion are not independent, therefore it is not straightforward to use quaternions in matrix computations. One option is to convert quaternions to rotation vectors [134]. Rotation vector $\vec{\mathrm{w}}_q$, $\vec{\mathrm{w}}_q = \theta \vec{e}$ represents rotation of angle θ around unit vector $\vec{e} \in \mathbb{R}^3$.

The quaternion 4.1 is converted to a rotation vector $\vec{\mathrm{w}}_q$ with the following equations:

$$\theta = 2 \arctan \left(\frac{\|\vec{v}_q\|}{w} \right), \vec{\mathrm{w}}_q = \theta \frac{\vec{v}_q}{\|\vec{v}_q\|}. \tag{4.5}$$

A unit quaternion representing this rotation is [132]:

$$q = \left[\cos\left(\frac{\theta}{2}\right), \vec{e} \sin\left(\frac{\theta}{2}\right) \right]^T. \tag{4.6}$$

4.3 SUBJECTS AND MEASUREMENTS OF STUDY I

4.3.1 Subjects

Participants for study **I** were recruited from the clinical nutrition unit of Kuopio University Hospital, Kuopio, Finland. The recruitment period was from October 2008 to August 2010. The entry criteria consisted of patients being cleared for bariatric surgery at Kuopio University Hospital and willingness to take part in the present study. Previous knee or hip arthroplasty was an exclusion criterion. Each participant provided written consent to participate in this study after receiving detailed information about the study design. The Ethics Committee of the Kuopio University Hospital approved the study design.

At baseline, fifteen female and three male middle-aged obese adults aged between 30 and 63 years were recruited for this study. The baseline measurement for each subject was performed before the bariatric surgery. The follow-up measurements were performed 8.8 (SD 4.2) months after the surgery. Two subjects refused to participate in the follow-up measurements due to personal reasons. Two subjects failed to complete the tests at 1.2 m/s and 1.5 m/s walking speeds and one subject was excluded because ground reaction force data from the follow-up measurement was lost. The characteristics of the 13 participants (ten female and three male) included into the final evaluation are shown in Table 4.1. From these subjects, one failed to complete tests at 1.5 m/s and one subject's camera data was lost at the 1.2 m/s walking speed. At baseline all 13 subjects were severely or morbidly obese, i.e. the body mass index (BMI) was > 35 kg/m^2 (range 36.4-49.7). Average weight loss was 26.7 kg (SD 9.2 kg), corresponding to 21.5% (SD 6.8%) of the initial weight.

The self-reported disease-specific joint pain was assessed using the Western Ontario and McMaster Universities (WOMAC) Osteoarthritis Index [135]. Four subjects reported mild knee pain (Table 4.1).

The knee and pelvis radiographs were taken and evaluated using Kellgren-Lawrence grading [136], in which grade ≥ 2 was regarded as knee or hip OA. According to the radiographic score of the subjects, none had hip OA and three subjects had mild knee OA (KL 2) and one subject had moderate knee OA (KL 3) (Table 4.1).

Table 4.1: Subject characteristics (n = 13). Values are means (SD) and knee and hip radiographic KL-gradings are number of subjects.

Variables	
Age (years)	45.5 (10.3)
Weight (kg)	
Baseline	123.3 (19.1)
Follow-up	96.6 (16.2)
BMI (kg/m^2)	
Baseline	42.2 (3.9)
Follow-up	33.1 (3.8)
WOMAC[1]	
Pain (0-100 (mm))	
Baseline	15.8 (11.6)
Follow-up	9.1 (4.5)
Knee/hip KL-grading[2]	
0	5/12
1	4/1
2	3/0
3	1/0
4	0/0

[1] Those who reported knee pain (n = 4), WOMAC (Western Ontario and McMaster Universities Arthritis Index)

[2] The more severely affected side, Kellgren-Lawrence (KL) grade.

4.3.2 Measurements

Walking speed was measured using a pair of photo-cells located 2.5 meters apart on either side of the force platforms. The data collection was initiated when the subject passed the first photo-cell. This, along with the sufficient calibration volume of the camera system, enabled the recording of 3D-kinematics of four consecutive steps.

The subjects were given enough time for warm-up and to become familiar with the experiment protocol. Subsequently, the subjects walked barefoot at pre-determined gait speeds, 1.2 m/s and 1.5 m/s, along the walkway. Six trials at both speeds were recorded, with the trial order being randomized. A trial was discarded if both feet did not hit the force platforms or if purposeful targeting on the platforms was observed. Furthermore, gait speed had to be within ±5% of the target speed.

Subjects wore tight-fitting spandex trousers and a shirt. The markers were attached onto the skin of the feet and onto the suit. Marker placement was based on a modified Helen Hayes marker set, where three markers per segment were mounted. Marker locations were the posterior heel, first and fifth metatarsal heads, lateral malleoli, tuberositas tibiae, lateral knee joint space, gastrocnemius muscle, biceps femoris muscle, trocanter major, spina iliaca anterior superior and lumbar vertebra.

4.3.3 Data analysis

Motion tracking was performed using a seven-segment model. The model was similar to the one presented in study **II**, with segments being the pelvis, both thighs, shanks and feet. Relative segment masses were taken from the literature [137]. Joint angle and moment graphs were calculated for all gait trials. Clear outliers were removed based on visual inspection of the graphs. Parameter values were determined from the remaining trials. The value of the parameter for a subject was defined as the mean of these values.

Cadence parameters were calculated using kinematic data. To determine step width, we defined two lines which connected consecutive heel contact points of the same foot. The step width was determined as the distance between a line and the opposite heel contact point.

The nonparametric Wilcoxon signed rank test was used to determine the differences between the baseline and the follow-up measurements on the computed variables. The level of significance was set at $p < 0.05$.

4.4 METHODS APPLIED IN STUDY II

4.4.1 Multisegment model and its kinematic state

A multisegment model representing human lower body was defined in 3D space. In this arrangement, model segments have fixed dimensions and they are articulated together. The model can be backprojected onto the image planes. Figure 4.2 shows a sample of the model and its backprojections. Points where the next segment is articulated are defined in segment reference frames. Similarly, fixed points are defined to the locations corresponding to placement of reflective markers on the subject. These anchor points are used in the observation model of the UKF (section 4.4.2). Model dimensions are defined in calibration measurements. Anchor point locations are adjusted based on the marker placement of each measurement.

The model is parametrized as a hierarchical model: the position ($\vec{r}_0$) and the orientation (q_0) of a base segment are defined in a laboratory reference frame and the positions of other segments are determined by relative quaternions and joint points. In addition to model geometry, only the base segment pose and joint angles are needed in order to define the pose of all the segments.

The velocities and accelerations of the segments are also of interest. Therefore, the state vector x of the model is defined as:

$$\begin{aligned} \mathrm{x} = \Big[\ & \vec{r}_0\ q_0\ q_{j1}\ \cdots q_{jN}\ \vec{v}_0\ \vec{\omega}_0\ \vec{\omega}_{j1}\ \cdots \vec{\omega}_{jN} \cdots\ , \\ & \vec{a}_0\ \vec{\alpha}_0\ \vec{\alpha}_{j1}\ \cdots \vec{\alpha}_{jN}\ \Big]^T . \end{aligned} \tag{4.7}$$

Vectors $\vec{v}_0$ and $\vec{a}_0$ are the linear velocity and acceleration of the base segment. Quaternion q_0 and vectors $\vec{\omega}_0$ and $\vec{\alpha}_0$ are the orientation and the angular velocity and acceleration of the base segment in the laboratory reference frame. Subindexes $j1...jN$ refer to the joints of the model. Relative quaternions $q_{j1}...q_{jN}$ describe the orientation difference between adjacent segments, and the corresponding angular velocities and accelerations are stacked in the vector.

The state and the model geometry unambiguously define the kinematics of each segment. Hierarchical modeling makes it possible that the degrees of freedom of joints are constrained, e.g., by replacing a quaternion by a single angle and a fixed rotation axis.

When calculating sums and differences of vectors of the form (4.7), quaternion parts have to be treated by quaternion multiplications.

Let the sum and subtraction of state vectors x_1 and x_2 be [132]:

$$\mathrm{x}_1 \oplus \mathrm{x}_2 = \begin{bmatrix} \vec{r}_1 + \vec{r}_2 \\ q_2 q_1 \\ \vec{v}_1 + \vec{v}_2 \\ \vec{\omega}_1 + \vec{\omega}_2 \\ \vec{a}_1 + \vec{a}_2 \\ \vec{\alpha}_1 + \vec{\alpha}_2 \end{bmatrix} , \quad \mathrm{x}_1 \ominus \mathrm{x}_2 = \begin{bmatrix} \vec{r}_1 - \vec{r}_2 \\ q_2^* q_1 \\ \vec{v}_1 - \vec{v}_2 \\ \vec{\omega}_1 - \vec{\omega}_2 \\ \vec{a}_1 - \vec{a}_2 \\ \vec{\alpha}_1 - \vec{\alpha}_2 \end{bmatrix} \tag{4.8}$$

The quaternions in the state vectors are converted to rotation vectors using procedure (4.5). Other parts of the state vector remain unchanged in the conversion. The conversion is denoted $\vec{\mathrm{w}} = \mathrm{Rotvec}\,(\mathrm{x})$. The opposite conversion is carried out with equations (4.6), and it is denoted $\mathrm{x} = \mathrm{Quat}\,(\vec{\mathrm{w}})$.

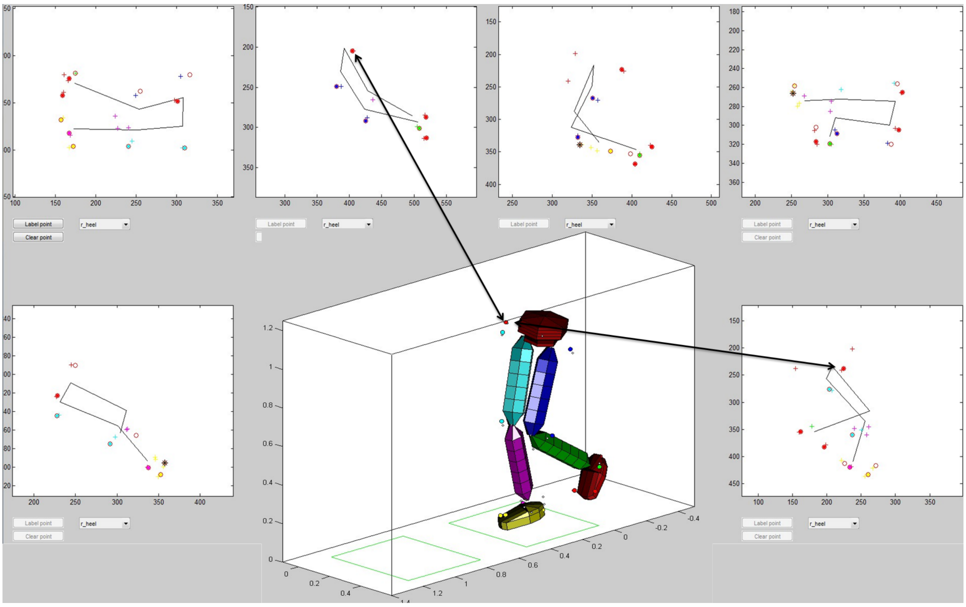

Figure 4.2: Lower body model and its backprojections on image planes of six cameras. A screenshot from graphical user interface implemented in MATLAB environment.

4.4.2 Unscented Kalman filter using quaternions

In this section, an algorithm used for time-varying estimation of the multisegment model state (4.7) is presented. The algorithm is based on the Kalman filter (KF) [51] and unscented transformation (UT). The algorithm is called the unscented Kalman filter (UKF) [138].

The publications of Särkkä and Hartikainen [139], [140] served as references when formulating the algorithm. The handling of quaternions in the UKF is based on the work described in [134].

The novel contribution of the proposed filter lies in the state evolution model of the UKF. In the linear KF and in the EKF, an evolution model $f(\cdot)$ is applied at a time step k to the previous estimate $\hat{\mathrm{x}}_{k-1}$, $\hat{\mathrm{x}}_{k|k-1} = f\left(\hat{\mathrm{x}}_{k-1}\right)$, and a predicted estimate $\hat{\mathrm{x}}_{k|k-1}$ is yielded. In the UKF, the UT is performed for $\hat{\mathrm{x}}_{k-1}$, and an evolution model is applied for a set of sigma points. (see the Appendix of publication **II** for details).

Next, the implementation of the proposed evolution model $(f(\cdot))$ for a single state vector is presented.

State evolution model with contact constraint

The evolution model is a Wiener Process Acceleration (WPA) model [141], where the derivative of acceleration is modeled as Gaussian noise. This model is used when the contact constraint is not triggered.

For linear motion the state evolution model is as follows:

$$\vec{r}_k = \vec{r}_{k-1} + \vec{v}_{k-1}\Delta t + \vec{a}_{k-1}\frac{(\Delta t)^2}{2} \tag{4.9}$$

$$\vec{v}_k = \vec{v}_{k-1} + \vec{a}_{k-1}\Delta t \tag{4.10}$$

$$\vec{a}_k = \begin{cases} \vec{a}_{k-1}, & \text{constraint not triggered} \\ \vec{a}_{\text{const}}, & \text{constraint triggered} \end{cases} \tag{4.11}$$

When the contact constraint is triggered, an acceleration impulse is inserted to $\vec{a}_k$. The acceleration impulse is defined depending on what type of collision is intended to be modeled. In the case of floor contact, acceleration can be chosen such that it stops the motion of the model towards the floor, during one or several time intervals Δt.

When handling angular motion, rotation vectors are used [134]. First, rotations caused by angular velocity and angular acceleration during the time interval Δt are extracted from the input state $\hat{\mathrm{x}}_{k-1}$,:

Angular velocity:

$$\text{angle:}\quad \theta_\omega = \|\vec{\omega}_{k-1}\|\,\Delta t \tag{4.12}$$

$$\text{axis:}\quad \vec{e}_\omega = \frac{\vec{\omega}_{k-1}}{\|\vec{\omega}_{k-1}\|}, \tag{4.13}$$

and angular acceleration:

$$\text{angle:}\quad \theta_\alpha = \|\vec{\alpha}_{k-1}\|\,\frac{(\Delta t)^2}{2} \tag{4.14}$$

$$\text{axis:}\quad \vec{e}_\alpha = \frac{\vec{\alpha}_{k-1}}{\|\vec{\alpha}_{k-1}\|} \tag{4.15}$$

Corresponding quaternions q_ω and q_α are constructed using equation (4.6). These quaternions are combined with the quaternions in $\hat{\mathrm{x}}_{k-1}$ by quaternion multiplications [134]:

$$q_k = q_\alpha\,(q_\omega q_{k-1}) \tag{4.16}$$

For angular velocity and acceleration, the WPA model is used.

$$\vec{\omega}_k = \vec{\omega}_{k-1} + \vec{\alpha}_{k-1}\Delta t \tag{4.17}$$

$$\vec{\alpha}_k = \vec{\alpha}_{k-1} \tag{4.18}$$

Initialization of the algorithm

The initial state estimate $\hat{\mathrm{x}}_0$ and its covariance $\mathbf{P}_0$ have to be set before the filtering. The initial pose of the model can be defined by a time frame where a sufficient number of observations are identified, and checked visually. Initial velocities and accelerations may be set to zero. The matrix $\mathbf{P}_0$ should be positive-definite. One simple option is to use a diagonal matrix, with elements of the magnitude $10^{-4}...10^{-1}$ on the diagonal.

The algorithm at time step k

Unit quaternions are used for orientation presentation in the state vector. However, matrix calculations in the UKF are performed with rotation vectors. Therefore, the algorithm includes conversions between quaternions and rotation vectors. Matrices $\mathbf{\Sigma}$ and all the covariance matrices in the algorithm contain rotation vectors. Matrices $\mathbf{X}$ contain quaternions. Adjustable parameters of the UT are denoted by the scaling parameter c, weight matrix $\mathbf{W}$, and weight vector $\mathbf{w}$, see Appendix of publication **II** for details.

The algorithm of the filter is as follows:

Predict step: The state estimate $\hat{\mathrm{x}}_{k-1}$ and its covariance $\mathbf{P}_{k-1}$ from the previous time step are known. In the predict step, UT is performed for $\hat{\mathrm{x}}_{k-1}$.

First, matrix $\mathbf{\Sigma}_{k-1}$ is constructed:

$$\mathbf{\Sigma}_{k-1} = \sqrt{c}\begin{bmatrix}0 & \sqrt{\mathbf{P}_{k-1}} & -\sqrt{\mathbf{P}_{k-1}}\end{bmatrix} \tag{4.19}$$

A set of sigma points $\mathbf{X}_{k-1}$ is constructed by converting rotation vectors in $\mathbf{\Sigma}_{k-1}$ into quaternions and adding the mean to each point:

$$\mathbf{X}_{k-1} = \mathrm{Quat}\left(\mathbf{\Sigma}_{k-1}\right) \oplus \left[\hat{\mathrm{x}}_{k-1}, \cdots, \hat{\mathrm{x}}_{k-1}\right] \tag{4.20}$$

Next, the evolution model is applied to each sigma point and the predicted state estimate $\hat{\mathrm{x}}_{k|k-1}$ is calculated using propagated sigma points ($\mathbf{X}_{k|k-1}$).

$$\begin{aligned}
\mathbf{X}_{k|k-1} &= f\left(\mathbf{X}_{k-1}\right) && (4.21)\\
\hat{\mathrm{x}}_{k|k-1} &= \mathbf{X}_{k|k-1}\mathbf{w} && (4.22)\\
\widetilde{\mathbf{X}}_{k|k-1} &= \mathbf{X}_{k|k-1} \ominus \left[\hat{\mathrm{x}}_{k|k-1}, \cdots, \hat{\mathrm{x}}_{k|k-1}\right] && (4.23)\\
\mathbf{\Sigma}_{k|k-1} &= \mathrm{Rotvec}\left(\widetilde{\mathbf{X}}_{k|k-1}\right) && (4.24)\\
\mathbf{P}_{k|k-1} &= \mathbf{\Sigma}_{k|k-1}\mathbf{W}\mathbf{\Sigma}_{k|k-1}^{T} + \mathbf{Q}\ . && (4.25)
\end{aligned}$$

In equations (4.23) and (4.24), sigma points $\mathbf{X}_{k|k-1}$ are modified for the computation of predicted covariance $\mathbf{P}_{k|k-1}$. Matrix $\mathbf{Q}$ is the covariance of state noise; this will be explained later (4.33).

Update step:

$$\begin{aligned}
\mathbf{Z}_k &= h(\mathbf{X}_{k|k-1}) && (4.26)\\
\hat{\mathrm{z}}_k &= \mathbf{Z}_k\mathbf{w} && (4.27)\\
\widetilde{\mathbf{Z}}_k &= \mathbf{Z}_k - \left[\hat{\mathrm{z}}_k, \cdots, \hat{\mathrm{z}}_k\right] && (4.28)\\
\mathbf{S}_k &= \widetilde{\mathbf{Z}}_k\mathbf{W}\widetilde{\mathbf{Z}}_k^{T} + \mathbf{R} && (4.29)\\
\mathbf{K}_k &= \mathbf{\Sigma}_{k|k-1}\mathbf{W}\widetilde{\mathbf{Z}}_k^{T}\left(\mathbf{S}_k\right)^{-1} && (4.30)\\
\hat{\mathrm{x}}_k &= \hat{\mathrm{x}}_{k|k-1} \oplus \mathrm{Quat}\left(\mathbf{K}_k\left(z_k - \hat{\mathrm{z}}_k\right)\right) && (4.31)\\
\mathbf{P}_k &= \mathbf{P}_{k|k-1} - \mathbf{K}_k\mathbf{S}_k\mathbf{K}_k^{T} && (4.32)
\end{aligned}$$

The observation model $h(\cdot)$ comprises the articulated model and its backprojections onto camera image planes. Output vector of the observation model consists of 2D pixel coordinates of model anchor points. Consequently, matrix $\mathbf{Z}_k$ contains pixel coordinates of anchor points corresponding to each sigma point in $(\mathbf{X}_{k|k-1})$. Vector z_k consists of observed pixel coordinates of markers on camera image planes. Not all the markers are visible to all cameras in every time frame. Indexes corresponding to missing observations are set to zero in both $\mathbf{Z}_k$ and in z_k. The observation noise matrix $\mathbf{R}$ defines the expected uncertainty of the observations. By setting $\mathbf{R} = \sigma_{\mathbf{R}}^2 \mathbf{I}$, the variance of the observation noise $\sigma_{\mathbf{R}}^2$ is expected to be the same for all observations.

Matrix $\mathbf{S}_k$ is the covariance of the measurement residual, and the Kalman gain matrix $\mathbf{K}_k$ is used in calculating the updated state estimate $\hat{x}_k$ and its covariance $\mathbf{P}_k$.

Since a WPA model is used, and since the rotations are described by rotation vectors, the matrix $\mathbf{Q}$ is of the form [141]

$$\mathbf{Q} = \sigma_{\mathbf{Q}}^2 \begin{bmatrix} \frac{(\Delta t)^5}{20}\mathbf{I} & \frac{(\Delta t)^4}{8}\mathbf{I} & \frac{(\Delta t)^3}{3}\mathbf{I} \\ \frac{(\Delta t)^4}{8}\mathbf{I} & \frac{(\Delta t)^3}{3}\mathbf{I} & \frac{(\Delta t)^2}{2}\mathbf{I} \\ \frac{(\Delta t)^3}{3}\mathbf{I} & \frac{(\Delta t)^2}{2}\mathbf{I} & \Delta t\mathbf{I} \end{bmatrix}, \tag{4.33}$$

where $\mathbf{I}$ is an identity matrix, with size equal to the degrees of freedom of the model, and $\sigma_{\mathbf{Q}}^2$ is the selected noise variance, *state noise*. If different noise magnitudes are specified for the linear and angular parts, block $\mathbf{I}$ is stacked from two blocks that have their own $\sigma_{\mathbf{Q}}^2$ coefficients.

Filter parameters

Noise variances $\sigma_{\mathbf{Q}}^2$ and $\sigma_{\mathbf{R}}^2$ determine the behavior of the filter. The smaller $\sigma_{\mathbf{R}}^2$ is, the more the observations of the current time step are weighted in the estimation i.e. estimates may be affected by noise in the data. On the other hand, small state noise variance $\sigma_{\mathbf{Q}}^2$ leads to estimates that obey more strictly the state evolution model. In the case of the WPA model, this means that changes in estimated motions are slow.

Marker identification

Estimates of the state (4.7) determine the pose of all model segments. Therefore, the predicted state can be utilized in marker identification. Once the filter is properly initialized, the predict step gives a reasonable estimate for the model pose in the current time frame, and observations are identified before the update step, where the observations are needed.

4.4.3 Unscented fixed-interval smoother

The fixed-interval Kalman smoother consists of filtering and backward recursion phases. Backward recursion is implemented according to [139]. The matrices $\mathbf{C}_k$ and $\mathbf{P}_{k|k-1}$ used in the recursion are stored during the filtering for each time step k. Matrix $\mathbf{C}_k$ is the cross-covariance of $\hat{x}_k$ and $\hat{x}_{k|k-1}$:

$$\mathbf{C}_k = \mathbf{\Sigma}_k \mathbf{W} \mathbf{\Sigma}_{k|k-1}^T \tag{4.34}$$

Backward recursion consists of the computation of matrix $\mathbf{D}_k$ and the use of the filter estimate x_k and predicted estimate $\mathrm{x}_{k+1|k}$, to form the final estimate $\mathrm{x}_k^{\mathrm{smth}}$:

$$\begin{aligned}
\mathbf{D}_k &= \mathbf{C}_{k+1} \left(\mathbf{P}_{k+1|k} \right)^{-1} && (4.35) \\
\vec{d} &= \mathrm{Rotvec} \left(\mathrm{x}_{k+1}^{\mathrm{smth}} \ominus \mathrm{x}_{k+1|k} \right) && (4.36) \\
\mathrm{x}_k^{\mathrm{smth}} &= \mathrm{x}_k \oplus \mathrm{Quat} \left(\mathbf{D}_k \vec{d} \right) && (4.37)
\end{aligned}$$

The whole algorithm, consisting of filtering and smoothing phases, is referred to as the unscented Kalman smoother (UKS).

4.4.4 Reference algorithm

The extended Kalman filter in conjunction with multisegment models has been used for human motion tracking in several cases [50, 52, 54]. Usually, state models are similar to the WPA model; the motion is assumed to be smooth. In the validation measurements, an EKF with the WPA model as the evolution model was implemented as a reference method. The filter tuning parameters were the same in both the UKF and the EKF. After applying the EKF algorithm, an extended fixed-interval smoother was performed [142]. In the rest of this thesis, the EKF with the smoother is referred to as the extended Kalman smoother (EKS). The smoother was used in acceleration estimation. The trajectory estimates of the 3D points were examined after the filter step, without using the smoother.

4.5 MEASUREMENTS CONDUCTED IN STUDY II

4.5.1 Test device

In order to test the method with a single segment model, measurements using a test device were performed. The device was built for the testing of motion laboratory equipment accuracy [129]. The device consists of an aluminum rod (length 101 cm), and two horizontal steel rods (length 17 cm). The rods have reflective markers fitted on the both ends. The device has two plastic brackets for mounting of accelerometers (Fig. 4.3, left).

During the measurement, the test device was moved by hand. The rod was consecutively raised and then struck on a force platform. One-centimeter-thick foamed plastic carpet was used on the platform to soften the collisions. Four measurement sets of 50 seconds duration were performed. There were a total of 108 strikes conducted. The speed at which the rod was struck to the platform was varied to obtain acceleration peaks in a range from 0.5 g up to 6 g.

Contact was detected using the force platform. An accelerometer was mounted on the lower bracket of the device. After the measurements, acceleration data were re-sampled to 100 Hz and gravitational acceleration was subtracted from the time series.

The model of the test device was constructed by using the measured dimensions (Fig. 4.3, right). The model state was presented as a vector of the form (4.7). In this case, the model had only one segment and no joints. Camera observations of four markers on the rods served as input data for the motion tracking algorithm.

The kinematic parameters of the model were then estimated using the presented approach, i.e., a model-based unscented Kalman filter with the contact constraint and smoother. The extended Kalman filter was used as a reference method. In both methods, a fixed-interval smoother was executed after filtering.

The contact constraint in the study was implemented by inserting linear acceleration into the state estimate in such a way that downward motion of the model decelerated instantly. The acceleration inserted into the estimate at the floor contact (time instant k) in the UKF was $a_z(k) = -0.9\frac{v_z(k-1)}{\Delta t}$, where $v_z(k-1)$ is the vertical speed in the previous time frame and Δt is the step duration. The coefficient -1 instead of -0.9 would completely stop the downward motion in one time step. A coefficient smaller than one was selected to ensure that the rod did not bounce back from the floor. The WPA model (equations (4.9)-(4.11)) used in the UKF predict step transferred the effect of the modified acceleration to the velocity and to the position of the model. The smoothness of the Kalman filter estimate is adjusted by coefficients of two covariance matrices (see section 4.4.2). It can be noted that when the appropriate order of magnitude for the coefficients is found, estimation is not sensitive to slight changes in the coefficients. The values of covariances depend on the magnitudes of state vector elements and observation coordinates. In the results shown, the parameters used were $\sigma^2_{\mathbf{Q}} = 200$ and $\sigma^2_{\mathbf{R}} = 0.1$.

The re-sampled accelerometer signal and the estimated accelerations were transformed to the laboratory coordinates. Vertical components of the signal and the estimates were then analyzed. Acceleration peaks were detected from the signal and estimates, and peaks corresponding to each floor contact were compared.

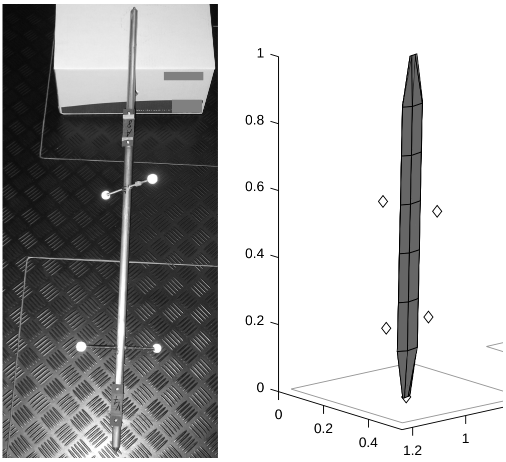

Figure 4.3: On the left: The test device with reflective markers and mounting brackets for accelerometers. On the right: Model of the test device. Model anchor points (◇) are defined to correspond to marker locations.

4.5.2 Lower body model

Measurements of human walking were performed to test the motion and acceleration estimation with a multisegment model. Two series of measurements were performed with two adult subjects, and twenty gait trials, each with one heel strike were analyzed.

Gait speeds of 1.0 m/s, 1.2 m/s, and 1.5 m/s, with ±5% tolerance were used. These speed ranges are widely used in clinical gait analysis.

Reflective markers were mounted on the skin and on tight-fitting spandex trousers using double-sided adhesive tape. We used the following marker locations: the first and fifth metatarsal heads, heel, lateral and medial malleolus, the lateral and medial epicondyle of the femur, greater trochanter, spina iliaca anterior superior, and sacrum. An accelerometer was mounted on the right foot using an adhesive bandage. The mounting location was on the medial side of the heel (Fig. 4.4, left).

Similarly to the test device measurements, camera observations served as input data in the estimation. Force platform signals were used for contact detection. The accelerometer signal was used as reference data.

A seven-segment model of the lower body was constructed, as described in section 4.4.1: the pelvis segment was used as the base segment and the pose of the other segments was defined through joint angles (4.7). Anchor points were defined to correspond to marker locations (Fig. 4.4, right). The model segment lengths, joint point positions, and accelerometer positions were determined in a calibration measurement, where the subject stood in a neutral position so that good visibility of the markers to the cameras was ensured. A set of three markers were attached to the accelerometer case in a calibration measurement. Thus, the position and orientation of the accelerometer with respect to the foot segment could be determined. The same model was used when performing the proposed method and the reference method.

The contact constraint was implemented by inserting an acceleration impulse into the state of the seven-segment model. The magnitude of the vertical acceleration impulse was $-c\frac{\vec{v_z}(k-1)}{\Delta t}$, where $\vec{v_z}(k-1)$ is the velocity of the foot segment prior to the floor contact. Coefficient c in the gait measurements was varied. The quantitative results reported were obtained using $c = -0.9$ with the filter parameters being $\sigma_{\mathbf{Q}}^2 = 10$ and $\sigma_{\mathbf{R}}^2 = 0.1$.

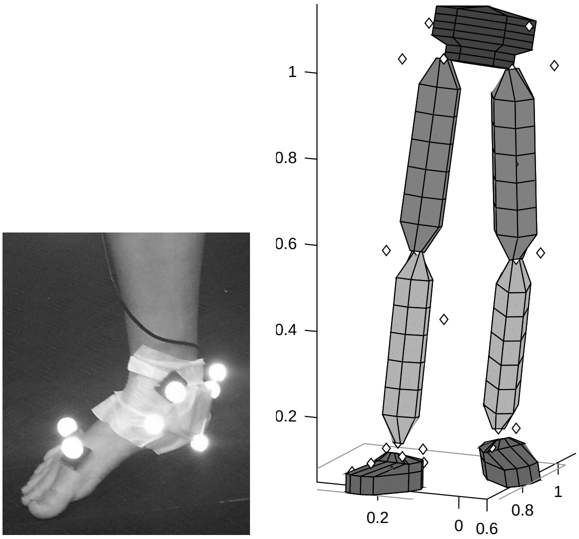

Figure 4.4: On the left: an accelerometer mounted on the foot of the subject. In the calibration setup, additional sets of markers are attached on the accelerometer. On the right: model used in human motion tracking.

4.6 METHODS AND MEASUREMENTS APPLIED IN STUDY III

4.6.1 Measurement setup

The inertial sensors used in the measurements are manufactured by Xsens Technologies (Enschede, Netherlands). The model of these wireless sensors is Xsens MTw (1st generation). The sensors were used to capture the motion of the lower body, spine and head. Sensor locations on the spine were chosen according to Ernst et al. [143]. They found that the spinal processes of the three thoracic vertebrae (T4, T7 and T10) and two lumbar vertebrae (L1 and L4) are located at the same relative distances along the distance between C7 and the PSIS-level, independent of subject body length. These locations are C7 0%, T4 21%, T7 39%, T10 54.1%, L1 70.9% and L4 86.1%. Locations for the sensors were marked on the skin and the lower edges of the sensors were placed on the marks. Each sensor was first attached on a slab of foamed plastic, which was then mounted on the skin using double-sided skin tape. Fig. 4.6(a) shows the measurement setup. The orientation data was recorded at 40 Hz sampling rate.

The study design of study **III** was approved by the Research Ethics Committee of the North Savo Hospital District. Informed consent was obtained from all individual participants included in the study.

4.6.2 Kinematic model of the spine and lower body for inertial sensor measurement

Kinematic model of human skeleton was constructed for the pose estimation of lower limbs and vertebrae. The body segments were modeled as rigid bodies, articulated together at joint center points. The model consisted of pelvis, the 24 vertebrae of the spine, head, thighs, calves and feet. The joint centers between the vertebrae were defined to the approximate center of inter-vertebral discs. The size of the vertebrae was scaled using the total length of the spine. The joint centers between the other segments were set based on the recommendations commonly used in reporting joint kinematics [144, 145]. All the joints had three degrees of freedom. The surface models of the segments were extracted and modified from OpenSim open-source library [146]. The kinematic model during spine rotation movement is visualized in Fig. 4.6(b). This shows the vertebra on which the lower edge of the sensor was mounted. The length and direction of a vector from the vertebra origin to the sensor location was adjusted based on soft tissue thickness of the subject, these vectors are visualized in Fig. 4.5. In this study, the length of the spine model was scaled using camera observations, the scaling can also be done using measured C7-PSIS distance.

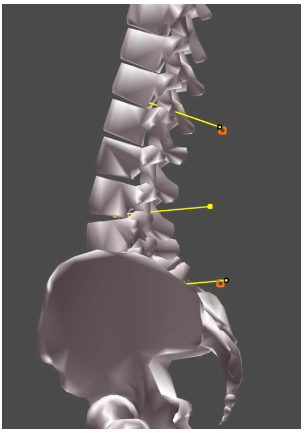

Figure 4.5: A snapshot of a kinematic model of lumbar spine. The yellow lines are vectors from vertebrae centers to a modeled sensor locations. Orange squares show the locations of the sensors on S1 and L1 estimates from camera-based motion capture.

Orientations of the model segments are presented using unit quaternions. Euler angles are used in reporting angle values; next the issues in calculating the angle values will be discussed.

Any unit quaternion can be converted to a rotation matrix unambiguously. The rotation matrix can be further converted to a set of Euler angles, the Euler angle values depend on the selected Euler sequence. For example, an Euler sequence $z - y - x$ means that the first Euler angle represents rotation around the x-axis of the reference coordinate system. The second Euler angle gives the rotation around the y-axis of the coordinate system rotated by the first angle. Correspondingly, the third angle represents the rotation around the z-axis of the coordinate system after the second rotation. By choosing a proper Euler sequence Euler angles can be used to describe angles in the three anatomical planes [144]. Since angle values depend on the Euler sequence, details of the sequence used should be described when reporting angles in 3D motion analysis [147]. Cognolato [82] suggested that the Euler sequence should be selected so that the axis around which the largest motion occurs should be first, and the axis with smallest range of motion should be last. In this study Euler sequences were chosen so that the anatomical angles are in the sequence flexion – lateral bending – spine rotation.

The kinematic model of the spine includes orientation of every vertebra, but only seven orientations are measured, hence interpolation of orientations is needed. A method called spherical linear interpolation (SLERP) [132] provides a robust and flexible way to compute the intermediate orientations. The SLERP gives the intermediate orientations along the shortest possible path.

Xsens sensors output the orientation from the sensor-fixed coordinate system to an Earth-fixed coordinate system [148]. The Earth-fixed coordinate system is a right-handed Cartesian system. The positive x-axis points to the Earth's magnetic North Pole and the z-axis points upwards, opposite to the gravity, and y-axis is defined by the right-hand rule. Sensor-fixed coordinate system is aligned with the plastic housing of the sensor.

The output quaternion of the sensor, q_S, transforms a vector $\vec{r}_\mathrm{S}$ in sensor coordinate system to the earth-fixed coordinate system, vector $\vec{r}_\mathrm{E}$. The coordinate transformation can be equivalently expressed using rotation matrix $\mathbf{R}_\mathrm{S}$.

$$\vec{r}_\mathrm{E} = \mathbf{R}_\mathrm{S}\vec{r}_\mathrm{S}, \tag{4.38}$$

or using quaternion q_S in multiplication

$$\begin{bmatrix} 0 \\ \vec{r}_\mathrm{E} \end{bmatrix} = q_\mathrm{S} \begin{bmatrix} 0 \\ \vec{r}_\mathrm{S} \end{bmatrix} q_\mathrm{S}^*, \tag{4.39}$$

where vector $\vec{r}_\mathrm{S}$ is concatenated by zero, and multiplied with quaternions q_S^* and q_S, respectively.

4.6.3 Calibrating model pose using inertial sensor data

Calibration was performed based on Roetenberg et al. [149]. During the calibration measurement, the subject was instructed to adopt a certain posture. The calibration posture in this study was a neutral standing posture, legs should be shoulder width apart and the spine naturally curved.

In order to calibrate, orientations of the sensors at calibration are defined in the Earth-fixed coordinate system. This set of orientations represents the supposed posture of the subject at the calibration.

In the spine measurements, it can be assumed that vertebrae at the neutral posture are aligned with each other, i.e., the lateral bending and rotation angles between the vertebrae are zero. However, the sagittal plane angles, i.e., the natural curvature of the spine, is preserved in the calibration procedure. Uncalibrated and calibrated orientations of the sensors at the calibration posture are illustrated in Fig. 4.7.

The angle around the global z-axis is called the heading. A heading for the whole model is needed in the calibration. This heading is determined based on the headings of individual sensors.

Next, the calibration procedure will be briefly presented. First, the calibration posture of the model is rotated to the heading measured at the calibration. Let q_i be the orientation of the i:th segment of the model. Quaternion q_h corresponds to the measured heading at the calibration. The heading of the model segment is set by quaternion multiplication

$$q_{i,\mathrm{h}} = q_\mathrm{h} q_i. \tag{4.40}$$

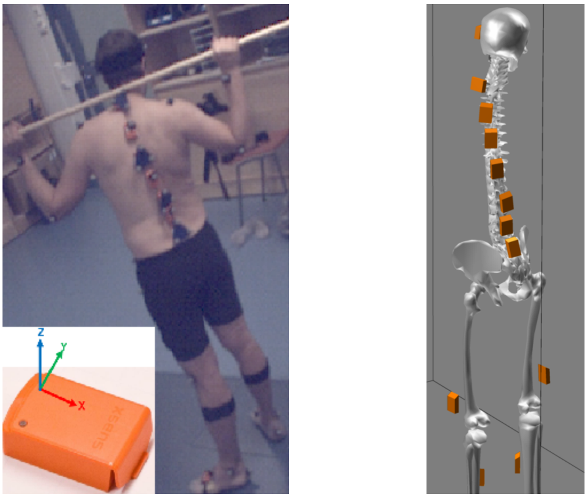

(a) (b)

Figure 4.6: The measurement setup (a) and kinematic model (b) during spine rotation movement. Single Xsens MTw sensor at lower left corner of (a) source: [148].

Let q_{S,t_0} be the measured orientation of the i:th segment at calibration time instant t_0. The difference between q_{S,t_0} and $q_{i,\mathrm{h}}$ is stored to the quaternion $\tilde{q}_i$,

$$\tilde{q}_i = q^*_{\mathrm{S},t_0} q_{i,\mathrm{h}}. \tag{4.41}$$

Now, the measured orientation q_S at any time instant is calibrated by quaternion multiplication

$$q_{\mathrm{S,c}} = q_\mathrm{S} \tilde{q}_i. \tag{4.42}$$

This calibration procedure addresses misalignment between a skin-mounted sensor and an underlying body segment.

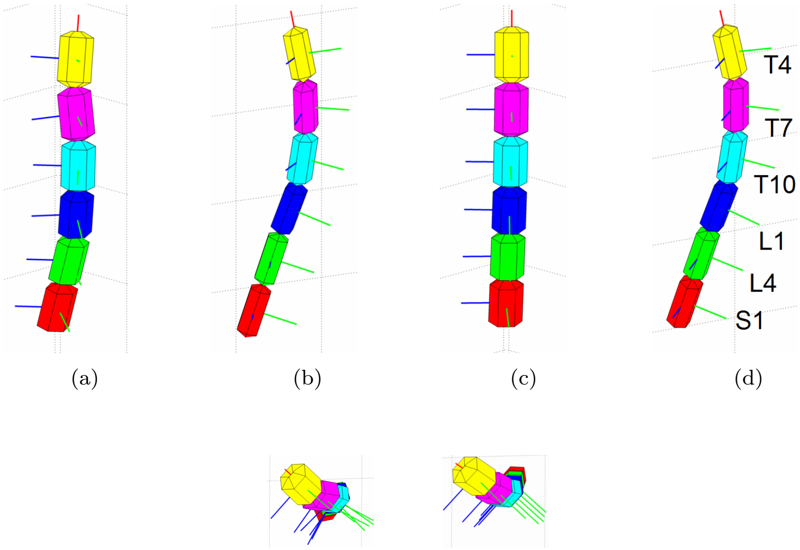

(a) (b) (c) (d)

(e) (f)

Figure 4.7: The effect of calibration on the orientations of the inertial sensors on the spine. Uncalibrated orientations (a), (b) and (e) and calibrated orientations (c), (d) and (f). Views from back, left and above.

5 Results

The following chapter summarizes the most important results of studies **I-III**. For additional details and complete results, see *ORIGINAL PUBLICATIONS.*

5.1 RESULTS OF STUDY I

As described in section 4.3, the study subjects were 18 obese individuals. The measurements were made prior to and in the follow-up after they had undergone bariatric surgery. No differences between the baseline and the follow-up were observed in swing time, in double support time or in stride length, whereas a significant decrease in step width was observed (Table 5.1). The hip flexion angle at initial contact decreased significantly at both gait speeds, but no significant changes were observed in knee joint angles (Table 5.2).

Both absolute and normalized values of knee joint moments are reported. Moments were normalized by dividing the absolute values by the product of subject's mass and height. Possible changes in gait geometry are reflected in the normalized values.

A significant decreases in the absolute values were observed in peak knee abductor moments, peak hip extensor moment and peak knee flexor moment (Table 5.3). The only significant difference noted in normalized moments was the increase in peak knee abductor moment during the early stance at a gait speed of 1.5 m/s.

Table 5.1: Cadence parameters (means (SD)) at gait speeds 1.2 m/s and 1.5 m/s. Significant p-values in bold.

Parameter	1.2 m/s			1.5 m/s		
	Baseline	Follow-up	p-value[1]	Baseline	Follow-up	p-value
Step width (m)	0.12(0.03)	0.09(0.03)	**0.001**	0.13(0.02)	0.09(0.02)	<**0.001**
Double support time (% Gait cycle)	14.6(1.8)	14.1(0.9)	0.570	13.2(1.3)	12.9(1.3)	0.420
Swing time (% Gait cycle)	37.6(1.3)	37.8(1.3)	0.470	40.0(1.0)	40.1(1.8)	0.970
Stride length (m)	1.29(0.09)	1.30(0.10)	0.850	1.42(0.09)	1.42(0.08)	0.850

[1] Wilcoxon signed-rank test

Table 5.2: Hip and knee angles (means (SD)) at gait speeds 1.2 m/s and 1.5 m/s. Significant p-values in bold.

Parameter	1.2 m/s			1.5 m/s		
	Baseline	Follow-up	p-value[1]	Baseline	Follow-up	p-value
Hip flexion angle at initial contact (°)	-32(6)	-26(4)	**0.010**	-32(7)	-27(5)	**0.020**
Peak knee flexion angle during early stance (°)	-22(5)	-19(5)	0.090	-24(7)	-22(6)	0.730
Knee flexion angle at initial contact (°)	-13(6)	-10(7)	0.150	-14(8)	-14(7)	0.790
Knee minimum flexion angle during stance (°)	1(9)	0(7)	0.380	5(9)	2(7)	0.300
Knee flexion angle at toe off (°)	-38(1)	-38(1)	0.470	-40(1)	-40(2)	0.970

[1] Wilcoxon signed-rank test

Table 5.3: Knee and hip joint absolute and normalized moments (means (SD)) at gait speeds 1.2 m/s and 1.5 m/s. Significant p-values in bold.

Parameter	1.2 m/s			1.5 m/s		
	Baseline	Follow-up	p-value[1]	Baseline	Follow-up	p-value
Peak knee abductor moment during early stance						
Absolute (Nm)	70(22)	57(19)	**0.016**	71(27)	62(19)	**0.043**
Normalized (Nm/(kg m))	0.32 (0.07)	0.32 (0.07)	0.791	0.32 (0.08)	0.36 (0.07)	**0.007**
Peak knee abductor moment during late stance						
Absolute (Nm)	64(22)	54(16)	**0.016**	61(20)	53(16)	0.092
Normalized (Nm/(kg m))	0.29 (0.09)	0.31 (0.07)	0.204	0.28 (0.08)	0.30 (0.08)	0.110
Peak knee extensor moment						
Absolute (Nm)	44(33)	33(22)	0.204	53(37)	44(29)	0.424
Normalized (Nm/(kg m))	0.19 (0.13)	0.18 (0.10)	0.970	0.23 (0.15)	0.25 (0.15)	0.733
Peak knee flexor moment						
Absolute (Nm)	-50(26)	-39(19)	**0.043**	-61(21)	-43(20)	**0.003**
Normalized (Nm/(kg m))	-0.24 (0.14)	-0.23 (0.12)	0.424	-0.29 (0.12)	-0.26 (0.13)	0.339
Peak hip extensor moment						
Absolute (Nm)	119(27)	89(20)	<**0.001**	162(34)	123(32)	**0.016**
Normalized (Nm/(kg m))	0.57 (0.15)	0.54 (0.10)	1.000	0.76 (0.15)	0.75 (0.18)	1.000
Peak hip flexor moment						
Absolute (Nm)	-93(27)	-86(55)	0.233	-105(28)	-100(63)	0.424
Normalized (Nm/(kg m))	-0.43 (0.13)	-0.48 (0.18)	0.791	-0.48 (0.10)	-0.55 (0.21)	0.622

[1] Wilcoxon signed-rank test

5.2 RESULTS OF STUDY II

5.2.1 Test device

3D trajectories

Reconstructions of the test device motion were inspected by creating a 3D animation. In order to compare the UKF and EKF filters, the trajectories of the model anchor points were compared. The reconstructed trajectories in the test device measurements revealed differences only during and after the impacts, as expected. The different nature of the EKF and UKF trajectory estimates are illustrated in Fig. 5.1, where vertical coordinates of the estimates and direct reconstructions during test device motion are shown. The residuals between directly reconstructed and estimated marker positions showed a base level of some millimeters, which was due to the definition of the model.

Peak accelerations

A sample of estimated and measured accelerations and detected peaks is presented in Fig. 5.2. The figure shows that the accuracy of the constraint used works most optimally at accelerations below 4 g. With larger accelerations, the measured signal is underestimated. However, the estimated peak values are closer to the measured acceleration over the whole range than estimates with the EKS algorithm. To evaluate the quality of peak acceleration estimates, a_{EKS} and a_{UKS} were plotted as a function of a_{measured} (Fig. 5.3). A least squares (LS) fit was performed on the estimates a_{UKS}. The LS line is $a_{\mathrm{UKS}} = 0.62a_{\mathrm{measured}} + 0.88$. The standard error of the fitting ranges from 0.26 to 0.52 in range $0.62\text{ g} < a_{\mathrm{measured}} < 6.00\text{ g}$. The error is visualized in Fig. 5.3 as dashed lines, which show that the error is relatively small.

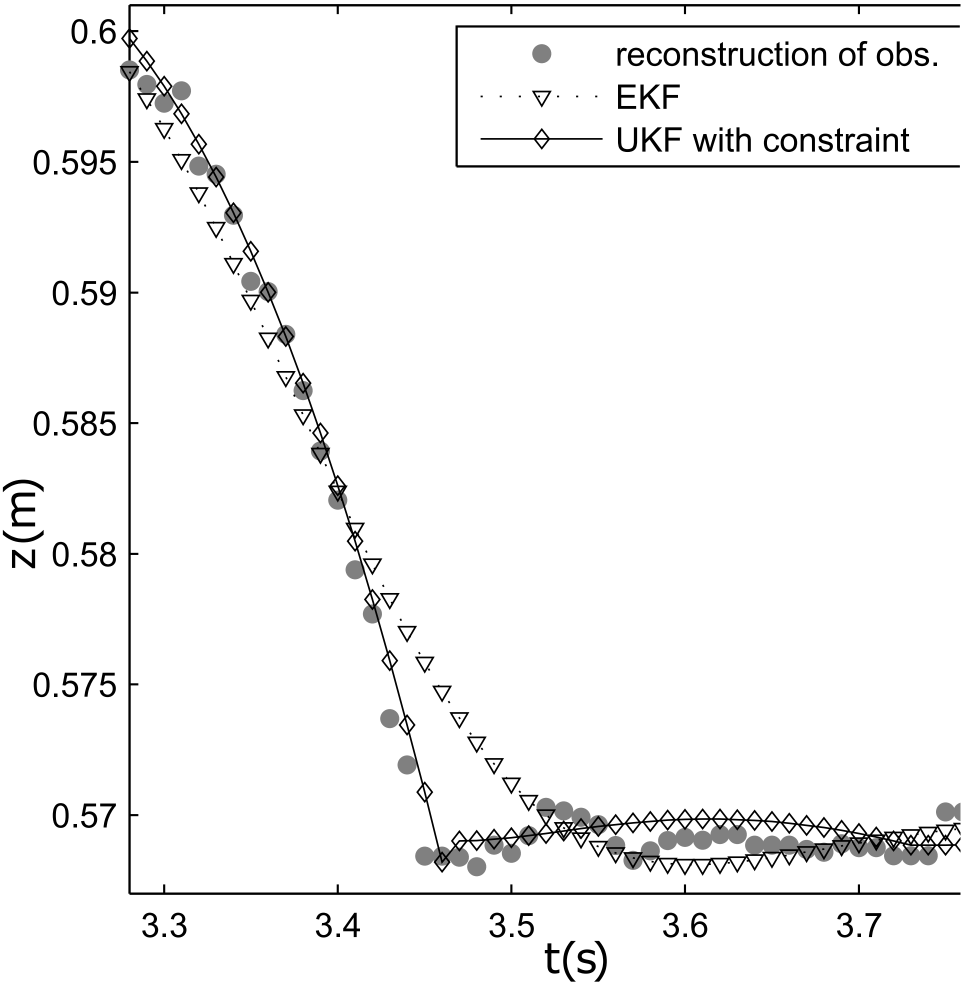

Figure 5.1: Example on z-coordinate estimates of a marker on the rigid rod (test device) during striking the rod tip on the force platform.

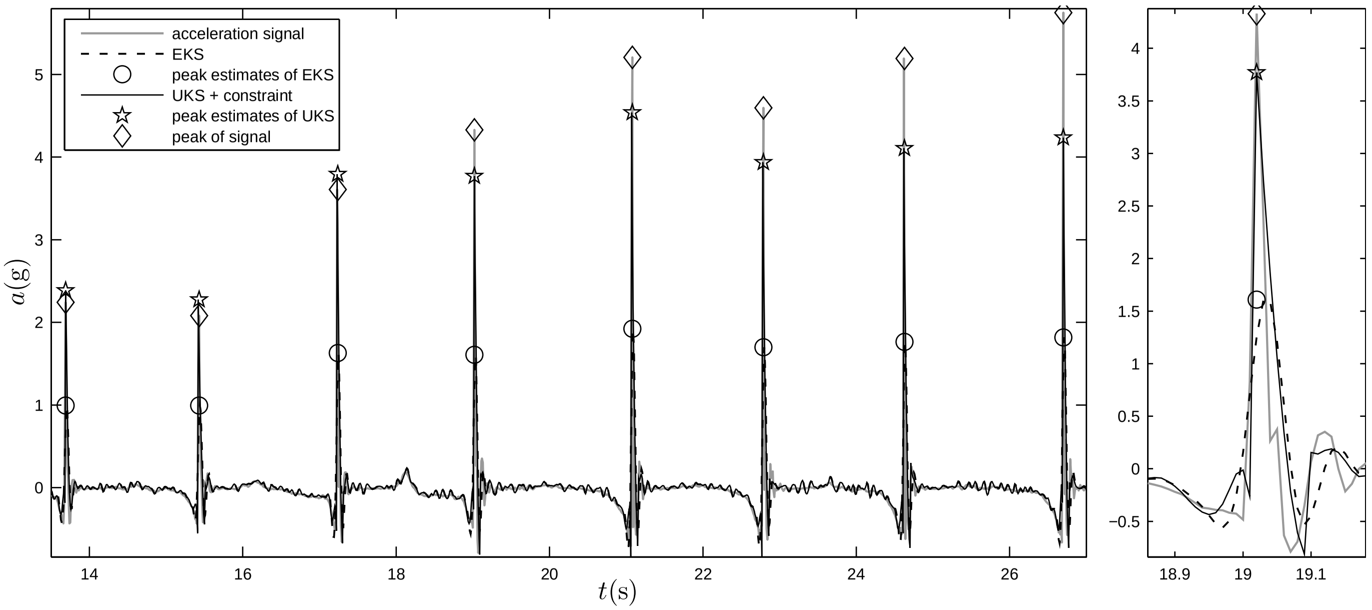

Figure 5.2: Measured and estimated accelerations in the test device measurement. On the left: Accelerations in a measurement where the device repeatedly strikes the force platform. On the right: A closer examination of the accelerations occurring during a strike on the force platform.

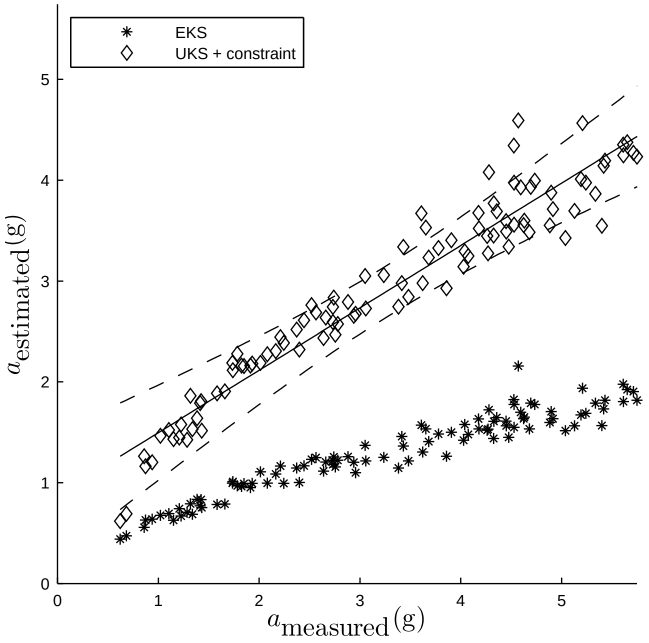

Figure 5.3: Estimated accelerations with respect to measured accelerations in the test device measurements. The equation of the fitted LS line is $a_{\mathrm{UKS}} = 0.62 a_{\mathrm{measured}} + 0.88$. Dashed lines represent the standard error of the fitting, which ranges from 0.26 to 0.53 in the range $0.62 \text{ g} < a_{\mathrm{measured}} < 6$ g.

5.2.2 Lower body model

3D trajectories

An example of the estimated and directly reconstructed trajectories during heel strike is shown in Fig. 5.4. The constraint in the proposed method keeps the heel point above the floor level, whereas the EKF estimate continues its path smoothly through the floor level. Fig. 5.5 reveals the vertical coordinates of the heel point estimates as a function of time in four gait trials. The figure illustrates that the constraint works systematically in the gait trials.

We calculated the difference in RMS errors between the trajectories that can be seen clearly in the heel marker during heel strikes. A window of 8 time steps around the heel strike was used in RMSE calculations. The mean RMS error of the heel strikes in the four gait trials of 1.5 m/s was 4.4 mm for the EKF method and 2.5 mm for the proposed method. During smooth motion, i.e. outside the heel contact window, differences in trajectories were very small and thus there was no difference in the RMS error (Table 5.4).

The effect of missing data was tested by removing observations of the heel and the ankle marker for a time interval of sixteen steps during heel strikes. The behaviour of the estimates is visualized by plotting the z-coordinates of the heel point in Fig. 5.6. The figure shows that the proposed method also works with incomplete data, since the contact constraint prevents the model from penetrating through the floor, whereas the EKF estimation is much worse due to the lack of data.

Estimates of anatomical knee and ankle angles were calculated using the EKF and UKF tracking results. The estimates were compared to the angle values based on direct reconstructions of markers. The knee joints had two degrees of freedom on EKF and UKF estimation; rotation was prevented. The angles during the gait cycle are shown in Fig. 5.10. The constraint affects most notably the knee adduction angle estimates.

Peak accelerations

The vertical components of measured and estimated accelerations of the foot were compared in the laboratory coordinate system. Figure 5.7 shows measured and estimated accelerations during a gait cycle. Figure 5.8 shows these accelerations during all the analyzed gait cycles. Peak accelerations at heel strike were extracted to compare estimates with measured accelerations. An LS fit was applied to the points a_{UKS} vs. a_{measured}, the fitted line is plotted in Fig. 5.9. The equation of the line is $a_{\mathrm{UKS}} = 0.51a_{\mathrm{measured}} + 0.59$. The standard error of the fitting is from 0.49 to 0.95. The range of accelerations was 1.89 g $< a_{\mathrm{measured}} <$ 4.98 g. The mean and standard deviation of the a_{measured} and both estimates are presented in Table 5.5.

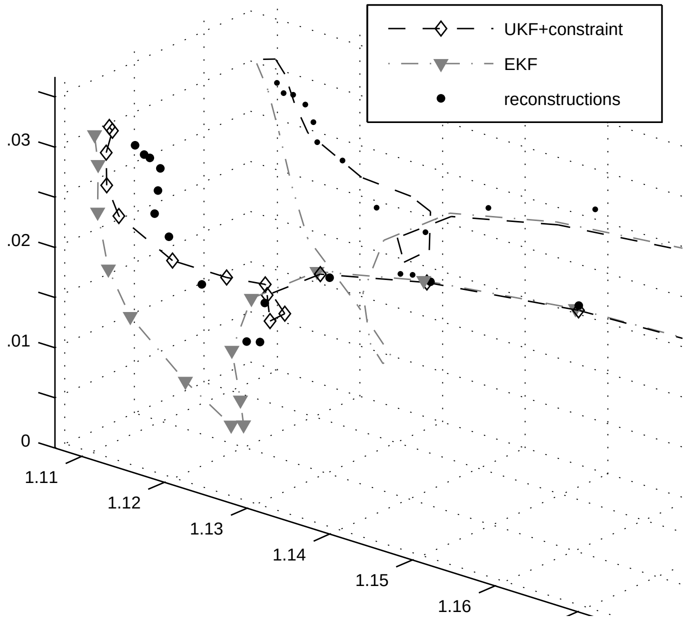

Figure 5.4: Trajectories of reconstructed and estimated heel markers during one heel strike event. Projections of the three trajectories on a vertical plane are also shown.

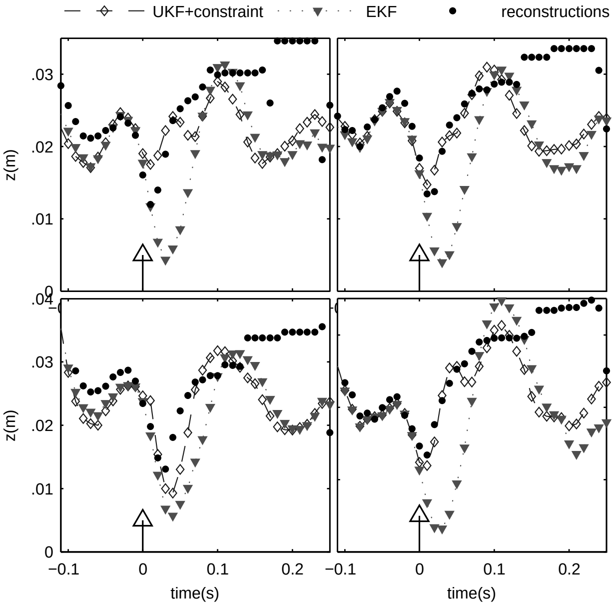

Figure 5.5: Z-coordinates of a marker on the right heel in four gait trials (Person 2, v_3). Graphs synchronized, detected heel strike at $t = 0$.

Table 5.4: Root mean square errors between directly reconstructed observations and estimates of marker trajectories of the EKF method and the UKF with the constraint method. Mean of four gait trials (Person 2, v_3), values in mm.

Data	RMSE (EKF)	RMSE (UKF + constraint)
Heel marker		
Heel strikes	4.4	2.5
Whole measurement	6.9	6.8
All markers on right foot		
Heel strikes	3.0	3.8
Whole measurement	7.5	8.1

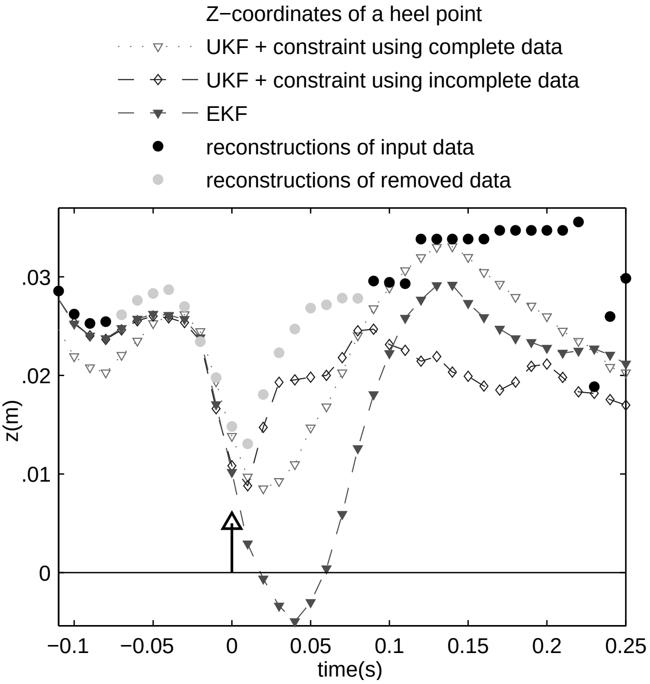

Figure 5.6: Effects of missing observations. A marker on the heel and a marker on lateral malleolus is removed from the input data at a time interval of 16 time steps. The removed data are visualized as gray dots. Heel strike at $t = 0$.

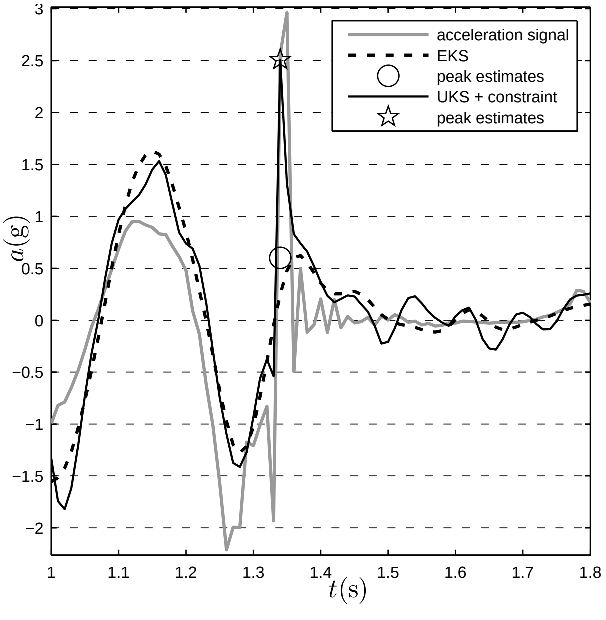

Figure 5.7: Measured and estimated vertical acceleration of the foot during gait. Initial contact occurs at 1.34 s.

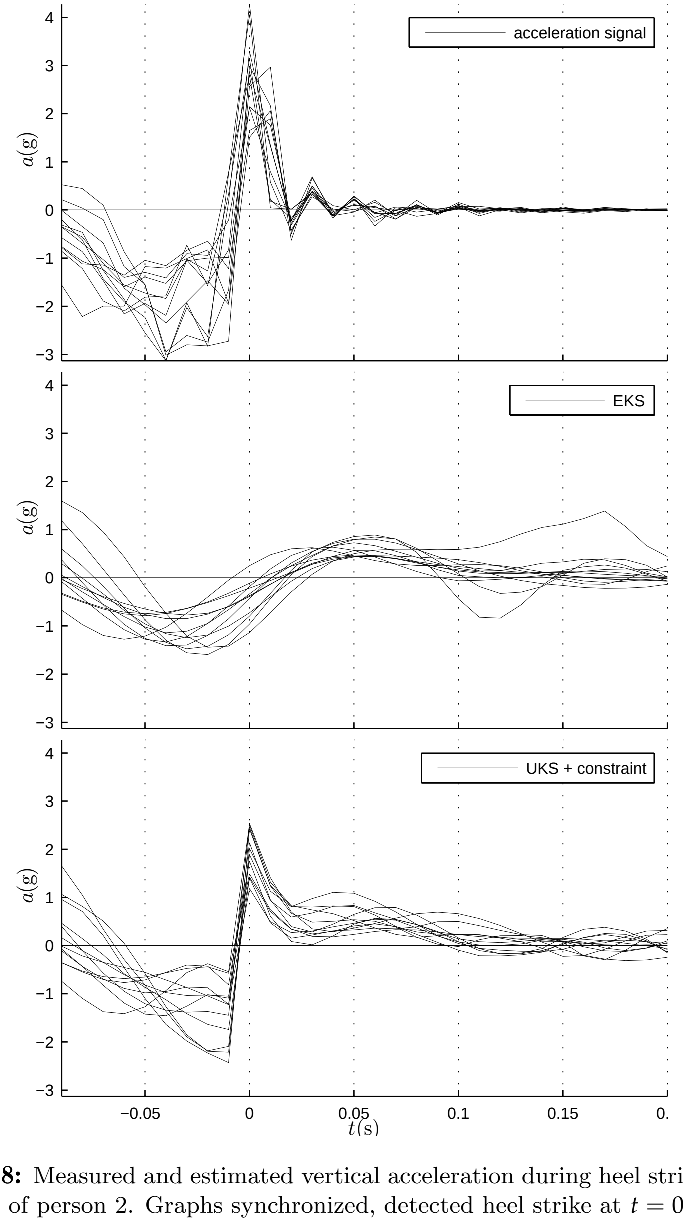

Figure 5.8: Measured and estimated vertical acceleration during heel strikes in the gait trials of person 2. Graphs synchronized, detected heel strike at $t = 0$.

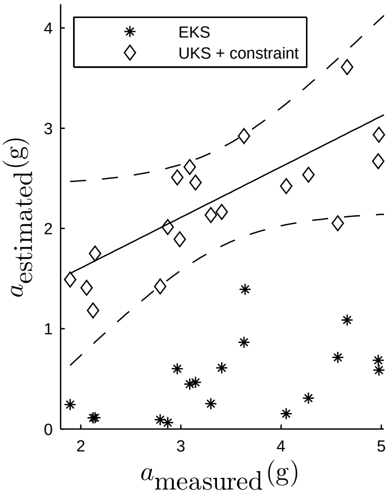

Figure 5.9: Estimated accelerations with respect to measured accelerations in gait measurements of two subjects. The equation of the fitted LS line is $a_{\text{UKS}} = 0.51a_{\text{measured}} + 0.59$. Dashed lines visualize the standard error of the fitting, which ranges from 0.49 to 0.95.

Table 5.5: Measured and estimated peak accelerations in gait experiments (means (±S.D.)). Measured a_{measured}, estimates by EKS (a_{EKS}) and the proposed UKS (a_{UKS}). Speed classes are $v_1 = 1.0$ m/s, $v_2 = 1.2$ m/s, $v_3 = 1.5$ m/s (±5%).

Speed	a_{measured}	a_{EKS}	a_{UKS}	Trials
Person 1				
v_1	4.07 (±0.64)	0.82 (±0.21)	2.69 (±0.73)	4
v_2	4.97 (±0.00)	0.64 (±0.07)	2.80 (±0.19)	2
v_3	3.36 (±0.39)	0.92 (±0.67)	3.22 (±0.85)	2
Person 2				
v_1	2.24 (±0.39)	0.14 (±0.07)	1.46 (±0.23)	4
v_2	2.87 (±0.56)	0.31 (±0.29)	2.13 (±0.51)	4
v_3	3.55 (±0.72)	0.06 (±0.25)	2.22 (±0.31)	4

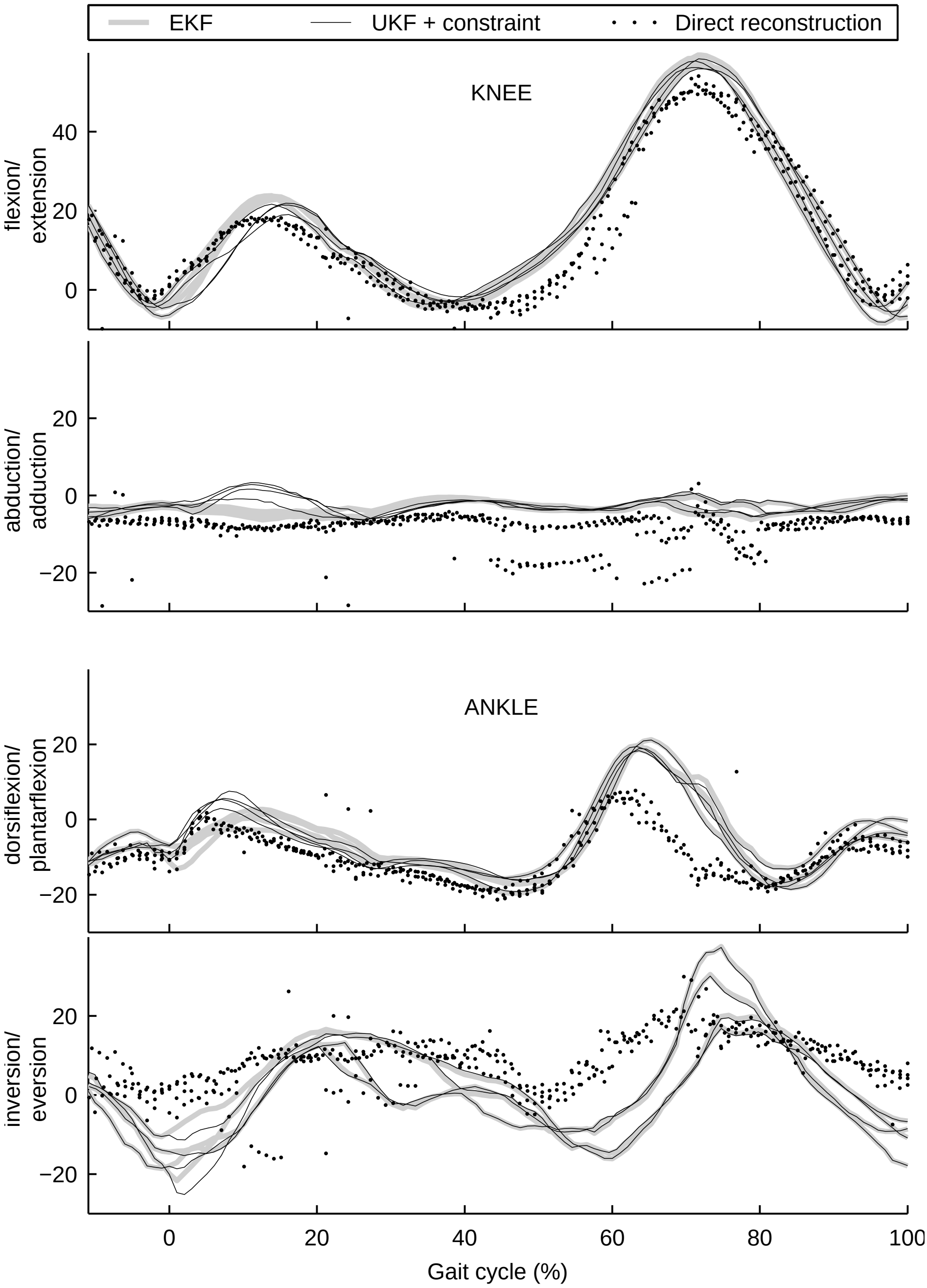

Figure 5.10: Estimates of the right knee and ankle joint angles. The contact constraint is triggered at the beginning of the gait cycle, (0%). Four gait trials (Person 2, v_3) are shown as example.

5.3 RESULTS OF STUDY III

In the study **III**, we measured and analyzed two different kinds of motion of the back, forward bending and spine rotation. In both cases, inter-vertebral angles and sensor-to-sensor distances by the kinematic modeling using inertial sensor measurement were compared with camera-based motion capture. Furthermore, the measurement of spinal shape during the movements was examined. A total of six sensors mounted along the spine were used for the shape estimation.

The 3D orientation of every vertebrae was estimated throughout the measurements. In Case 1, the sagittal plane angles of two different forward bending movements were examined. In Case 2, the angles between vertebrae were analyzed in the three anatomical planes. This analysis demonstrated the measurement of coupled movements.

5.3.1 Case 1: Forward bending movements

Two different forward bending movements were performed. The first movement was forward bending with a gymstick. The subject placed a gymstick on the neck level and he was instructed not to bend his neck. Bending was repeated six times. The duration of one repetition was approximately five seconds. The second movement was maximal forward bending, where the subject was instructed to bend the whole spine as much as comfortably possible.

Comparison of inertial sensor-based and camera-based estimates

The orientations of each vertebra were estimated using inertial sensor data and the kinematic model. The camera-based motion capture was used to obtain reference estimates for positions and orientations of the sensors S1, L1 and T7. The angles and distances between S1 and L1 vertebrae during the forward bending with the gymstick are shown in Fig. 5.11 and the corresponding estimates for the maximal bending are shown in Fig. 5.12.

The camera-based motion capture provided a reference for the distances between the sensors. Distance estimation based on inertial sensors depends on the model dimensions. The distance from the vertebra origin to the sensor location is a major factor affecting the model-based estimate. As demonstrated in Fig. 5.11 the distance between the sensors increased during the forward bending. The longer the vector between the vertebra and the sensor in the model, the greater the increases in the distances.

As can be seen from the graphs, camera-based estimates suffered from transient errors in marker detection. Thus, root mean square (RMS) difference between the estimates did not reach zero. We compared the accuracy during static and dynamic phases; the RMS differences during upright standing, during forward bending motion and during bent poses are shown in Table 5.6. At the maximal bending movement, these three situations are obvious. The RMS value for the ”bent pose” with the gymstick movement was calculated from 0.6 s interval around the most bent pose.

Spinal shape estimation

The angles between the vertebrae S1, L4, L1, T10, T7 and T4 are estimated using the sensors placed on the vertebrae during upright standing, i.e., at the calibration pose. The angle values during the bending with a gymstick are shown in Fig. 5.13,

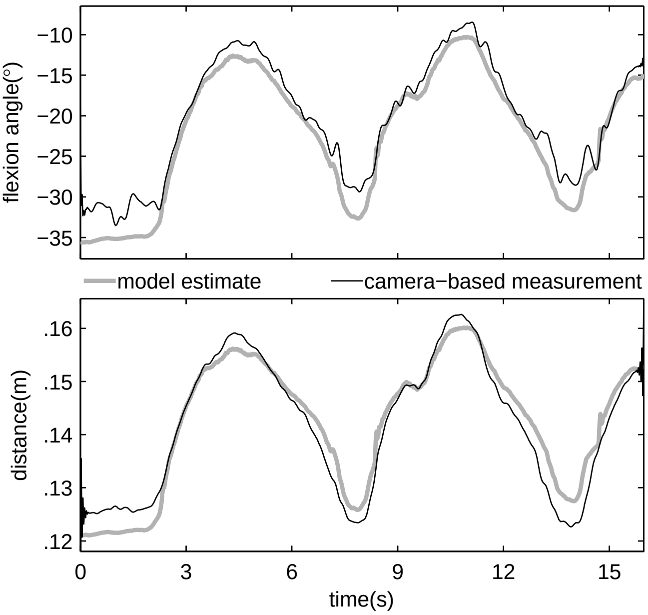

Figure 5.11: Estimates based on the inertial sensor data and modeling compared to camera-based measurement during forward bending with gymstick movement. Top: Relative flexion angle between S1 and L1 vertebra. Bottom: Distance between S1 and L1 vertebra.

Table 5.6: RMS differences between model estimates and camera-based measurements. The values were calculated during the initial pose, during forward bending motion and during bent pose.

	initial pose	during motion	bent pose
Flexion angle between L1 and S1 vertebrae (°)			
Gymstick bending	3.81	1.13	1.75
Maximal bending	3.79	1.30	2.51
Distance between L1 and S1 sensors (mm)			
Gymstick bending	4.3	1.3	2.8
Maximal bending	3.8	7.9	7.5

and during the maximal forward bending in Fig. 5.14. In these graphs, zero angle corresponds to the calibration pose. The graphs reveal that the largest difference between the two different bending movements was found in the angular motion between the L4 and L1 vertebrae. In addition, the angle between T10 and T7 revealed a major difference at thoracic spine between the two movements. During maximal forward bending this angle (T10-T7) was converted into flexion. In contrast, when bending with a gymstick this angle was converted into extension during the first repetition and it remained in extension during the rest of the repetitions. The 3D posture of the model at a certain time instant is illustrated by 3D animation implemented in MATLAB environment (MathWorks Inc.; MA, USA). Screen captures of animations during both movements are shown in Fig. 5.15.

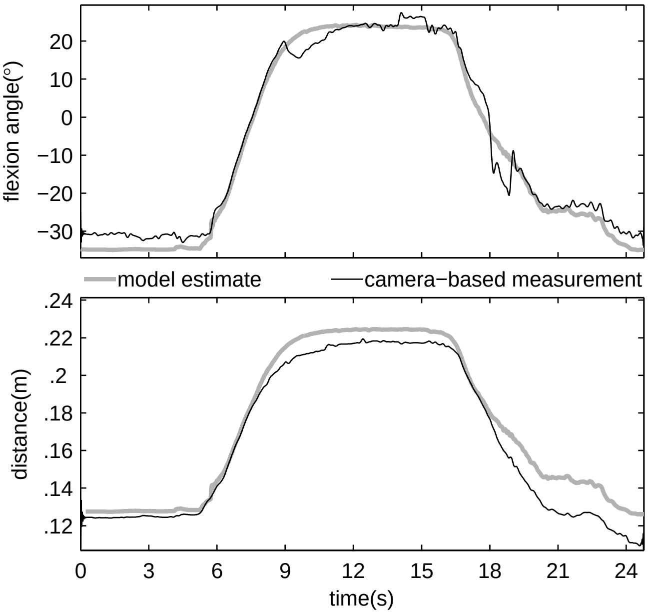

Figure 5.12: Estimates based on the inertial sensor data and modeling compared to camera-based measurement during maximal forward bending. Top: Relative flexion angle between S1 and L1 vertebra. Bottom: Distance between S1 and L1 vertebra.

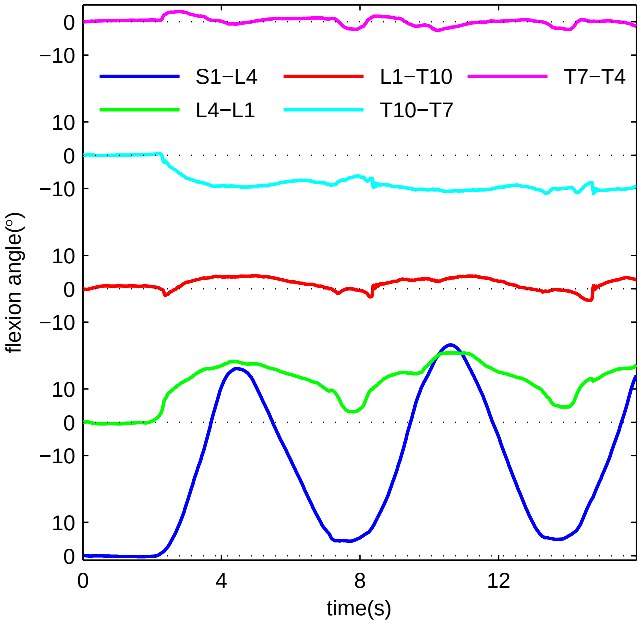

Figure 5.13: Flexion angles between the inertial sensors on lumbar and thoracic spine during bending with gymstick movement.

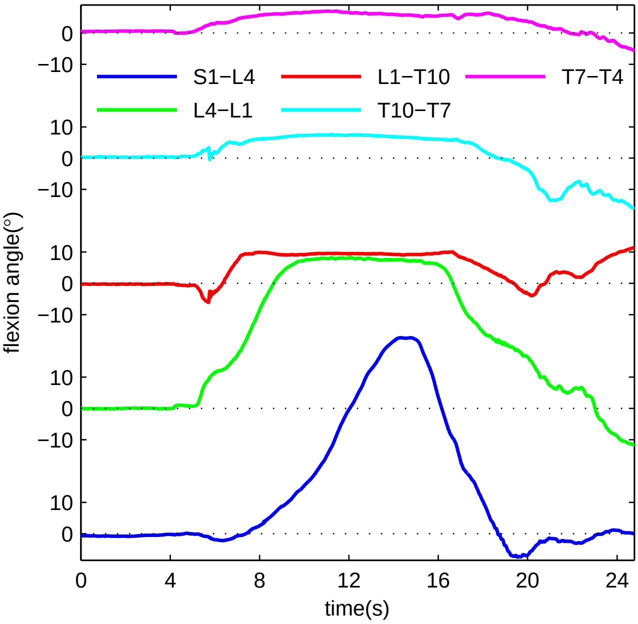

Figure 5.14: Flexion angles between the inertial sensors on lumbar and thoracic spine during maximal forward bending movement

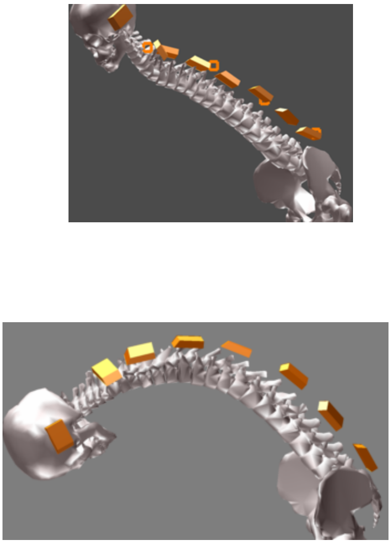

Figure 5.15: Screen captures of 3D model animation during the two forward bending movements. Left: a bending with the gymstick. Right: Maximal forward bending.

5.3.2 Case 2: Spine rotation movement

In this measurement, the subject placed a gymstick on the neck, above the C7 sensor, and he rotated his upper body four times consecutively.

Comparison of inertial sensor-based and camera-based estimates

During the rotation movement, the motion occurred in all three anatomical planes. The angles extracted from the inertial sensor data and kinematic modeling were compared with camera-based motion capture. The angle estimates between the sensors on S1 and T7 are shown in the top panel of Fig. 5.16. The corresponding distance estimates are shown in the bottom panel of Fig. 5.16.

In this movement, the RMS differences were computed during initial standing pose and during four repetitions. The RMS differences of every three angle components and sensor distances are shown in Table 5.7. The kinematic model provides values of range of motion (ROM) of the three angles. The ranges of rotational motion between S1 and T7 sensors in the four repetitions were 65.9, 67.9, 72.4, and 70.0 degrees.

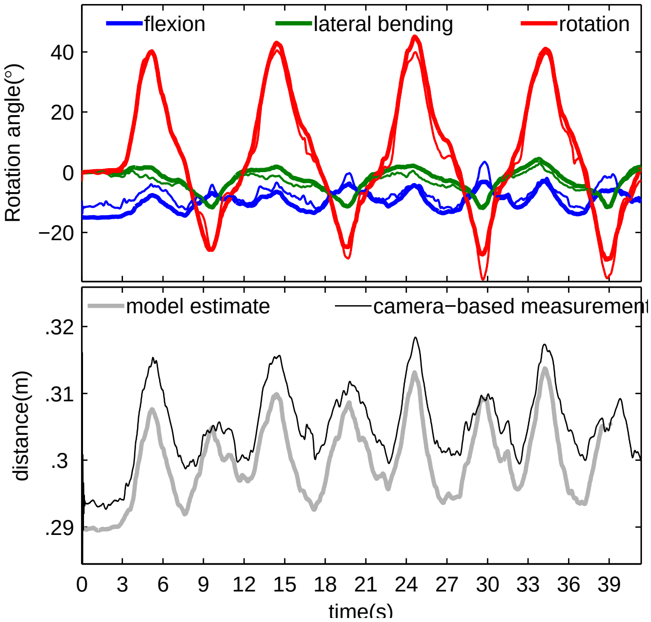

Figure 5.16: Estimates based on the inertial sensor measurement and kinematic model (thick lines) compared to camera-based measurement (thin lines) during the spine rotation. Top: Relative Euler angles between S1 and T7 vertebrae. Bottom: Distance between the same vertebrae.

Spinal shape estimation

Fig. 5.17 shows the rotation angles of the lumbar and thoracic vertebrae with respect to the sensor at S1. The angle S1-T10 shows a trend different from the other angles. The main reason for the trend was drifting of the T10 heading angle. The 3D motion of the model during the first two rotation cycles is provided as supplementary material of publication **III**.

Table 5.7: RMS differences between model estimates and camera-based measurements at the spine rotation movement. The values during initial pose and during four consecutive repetitions.

	initial pose	1. rep.	2. rep.	3. rep.	4. rep.
Angle between T7 and S1 vertebrae (°)					
rotation	0.59	2.77	4.48	3.64	2.04
lateral bending	0.20	0.61	1.13	0.75	0.58
flexion	2.94	2.28	2.27	1.94	1.69
Distance between T7 and S1 sensors (mm)					
	3.7	6.1	6.1	5.8	5.7

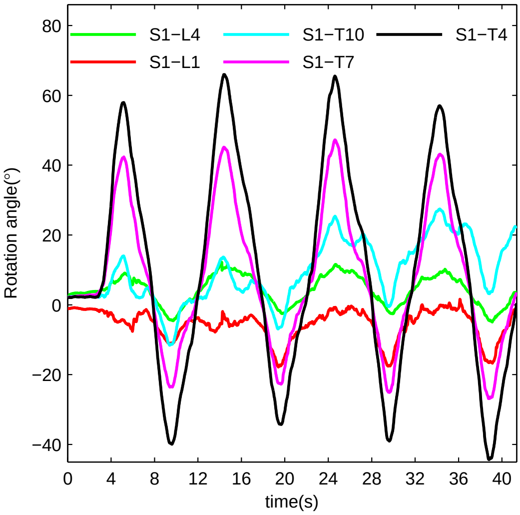

Figure 5.17: Rotation angles of the sensors at vertebra L4, L1, T10 and T7 with respect to the sensor at sacrum (S1) during repeated rotations of the spine.

6 Discussion

In this section, first, the results of the original publications will be discussed and in particular, the discussion of study **II** will be updated. In the last section, the various methods used in this thesis and novel methods in motion analysis are compared. In particular, the ways that each method can be utilized in the future will be examined.

6.1 GAIT CHANGES OF OBESE SUBJECTS IN BARIATRIC SURGERY-INDUCED WEIGHT LOSS

Publication **I** was the first study where inverse dynamics analysis was performed using the data collected in our in-house developed motion laboratory. Inverse dynamics calculations were implemented in MATLAB environment.

Absolute values of joint moments decreased as the weight declined, as was hypothesized. The change in peak knee abductor moment was -18.6% in early stance and -15.6% in late stance at a gait speed of 1.2 m/s following a 21.5% weight loss. At the gait speed of 1.5 m/s, the corresponding changes were -12.7% and -13.1%. These decreases were smaller than those previously reported when the amount of weight lost is taken into account; Hortobágyi et al. [28] described a -27.0% change in peak knee abductor moment in early stance after a weight loss of 33.6% in otherwise healthy subjects and Aaboe et al. [30] reported up to -13% in the peak knee abductor moment with a weight loss of 13.6% in knee OA subjects.

In contrast, the normalized values of sagittal plane moments revealed no significant changes, which means that absolute values of moments decreased in proportion to the weight loss. Most normalized peak knee abductor moments also remained statistically unchanged, with the only exception being in the peak abductor moment during early stance at a gait speed 1.5 m/s, which increased significantly. This would counteract the beneficial effects of weight loss on compressive loads being transmitted to the medial compartment of the knee. However, the importance of our finding is uncertain, because no effect on that moment was detected at a gait speed of 1.2 m/s. Thus, the results are rather consistent with those of Hortobágyi et al., who stated that there were no significant changes in normalized peak knee extensor or peak knee abductor moments [28] in otherwise healthy subjects. Furthermore, there is also evidence that in knee OA subjects extensive weight loss does not modify knee moments [150].

Hortobágyi et al. (2011) demonstrated that weight loss produced a substantial decrease in the absolute ankle plantar flexion moment at a standard walking speed (1.5 m/s), but the normalized ankle moments did not change after weight loss. Ankle joint parameters were not reported in this study **I**, since the markers on the forefoot could not be identified reliably in some situations. However, markers on the lateral malleoli were successfully tracked and thus the position of the ankle joint could be determined. The application point of the ground reaction force was reliably determined and thus the inverse dynamics calculations could be completed.

In study **I**, there were extensive inter-subject variations in the changes of moments. In some subjects, moment values increased, even though the mean value decreased significantly. This suggests that in the pre-surgery state, some individuals had made gait adaptations which lowered the joint moments at the baseline measurement due to neuromuscular adaptation [25].

The average decreases in step width were remarkable, 3 cm at gait speed 1.2 m/s and 4 cm at gait speed 1.5 m/s. It is possible that when individuals have more mass they have to place their feet wider apart in order to maintain their dynamic stability. The decrease in this value may also be explained by the reduced girth of the thighs. There are no earlier reports on the effects of weight loss on the step width. Browning and Kram [22] observed a greater step width in their obese compared to their normal-weight group. Thus, the association of larger weight and wider step width found in study **I**is consistent with the findings of Browning and Kram.

In our study, no changes in relative double support time or swing time were observed. These results are inconsistent with those of Browning and Kram [22], who found a greater relative stance time and swing time in the obese group compared to the normal-weight group. In addition, there was no change in stride length. However, an increase in stride length related to weight loss has been reported previously, even at a fixed gait speed [28]. No straightforward explanation for this inconsistency between studies was found.

We used fixed gait speeds to prevent speed affecting the gait parameters. If the subject's self-selected speed had been used, the speed might well have increased following the weight loss, as shown earlier by Aaboe et al. [30] and Hortobágyi et al. [28]. A higher speed would probably have increased the joint moments and thus counteracted the effects of the weight loss. Slower (1.2 m/s) and faster (1.5 m/s) speeds were used, which are estimates of normal gait speed for healthy individuals [151]. It was anticipated that the changes in gait parameters would be clearer when the subjects were performing a more demanding walking task, but no clear differences were observed.

Several limitations were recognized during study **I**. First, the validity of marker-based motion analysis is limited by the difficulties in marker placement especially in obese subjects, who have thick layers of soft tissue on most anatomic landmarks. Second, during weight loss, the thickness of soft tissue may decrease, and thus it is impossible to have identical marker placements in the follow-up measurements as used at the baseline.

The model-based method does allow for variations in marker placement, as the marker locations in the model can be modified. However, it is challenging to determine the marker locations in the model so that they would precisely represent the sites of the bony structures of the lower limbs. Thirdly, soft tissue and the spandex suit may cause movement artefacts. Finally, the absolute values of joint angles are error-prone, because static calibration measurements to determine the zero angles were not performed.

6.2 METHOD FOR ESTIMATION OF HUMAN BODY KINEMATICS BASED ON 2D MARKER TRAJECTORIES

The measurements conducted in study **II** demonstrated that the proposed method displays a difference to the EKF method when the constraint is triggered and during a few time steps after that, as expected. The estimated marker trajectories showed that when the direction of motion changed, the proposed method was able to track the change instantly, unlike the EKF method.

Acceleration estimation in test device measurements provided data for validation of the constraint. This constraint tended to underestimate large (> 4 g) accelerations.

However, the estimates were essentially closer to the real accelerations than estimates obtained by the extended Kalman smoother algorithm at contacts.

In the human gait measurements, the estimates of the proposed method and the EKF method revealed similar behaviour as the estimates in the test device measurements. Comparison of measured and the estimated accelerations showed that the extended Kalman smoother could not make reasonable estimates during heel strike. The acceleration inserted to the proposed method was based on the velocity of the foot before the heel strike. The velocity was extracted from the marker trajectories, thus an accelerometer is not needed in implementing the constraint.

Visual inspection of the acceleration estimates indicated that the estimates were smooth, and that high-frequency noise had been efficiently suppressed by fixed-interval smoother. Noise-free acceleration estimates are especially important when estimating joint loading without force measurements [152].

As the reference for acceleration estimates, skin mounted accelerometers were used, which represent a non-invasive way to measure accelerations on the leg [130]. Understandably, mounting of accelerometers on the skin introduces some artefacts [153]. Due to these artefacts, estimation of both impulsive and continuous segmental accelerations remains challenging. When force platform data is used along with the motion capture data, estimation of impulsive loadings on the knee level is sensitive to the low pass filtering of both the force and the kinematic data [154–156]. Kristianslund et al. [155] proposed that both forms of data should be processed with a same low-pass filter. Hewett et al. [156] questioned Kristianslund et al.'s conclusion; they pointed out that different kinds of movements should be examined, when selecting the filter cut-off frequency.

A fixed-interval smoother was used after the UKF and thus the data from the past and future could be utilized in the acceleration estimation. The backward recursion removes time lag from the estimates. The recursive estimation also suppresses high frequency noise. For online applications smoothing could be implemented using a fixed-lag smoother, which yields smoothed estimates with a lag of a few time steps. The filter algorithm was implemented in the MATLAB environment. Real-time implementation would be possible by utilizing a more efficient programming language and suitable hardware.

In addition to the acceleration estimation, the proposed model-based approach has several advantages in utilizing 2D marker observations. The model geometry, including anchor points, is projected to camera image planes. Projections of anchor points can be matched with 2D observations. Moreover, the UKF predict step enables online marker identification; the filter predicts the model pose in the current time step before any data from the time instant are used. The identified observations on the camera image planes can be directly used. Thus, markers seen by only a single camera are also utilized. In traditional methods, only 3D marker reconstructions are used, and thus at least two camera observations per marker are needed.

One benefit of using a hierarchical articulated model is that every segment does not need three markers. Two markers and a joint point are sufficient for the determination of the segment pose. The possibility to reduce the joint degrees of freedom is also useful, depending on the application and the quality of the marker data. For example, preventing the knee joint from rotating may be useful, since the actual rotation of the joint is small, and observation errors may cause false rotations [46]. The question of the best marker set still remains; recently so called six degrees-of-freedom sets have been proposed [157, 158].

The STA can be addressed by adjusting parameters of the UKF algorithm. In the filter update-step weight of each element of observation vector can be adjusted. Thus, the soft tissue artefacts can be reduced by putting smaller weights for the markers with large artefacts.

Reliable contact detection is essential when using contact constraints. Force platforms provide an accurate signal for detection. Detection based on camera observations is also possible, at least in offline applications. Thus, the use of constraint is not confined to the force platforms. Online detection using only optical information requires high accuracy in the whole system. The floor plane must be accurately localized in the calibrated space. The dimensions of the model, especially the foot segment, must be accurately defined.

6.3 INERTIAL SENSORS IN MOTION ANALYSIS

The two cases of study **III** revealed the capability of the proposed methodology at estimating the angles between vertebrae at lumbar and thoracic spine during forward bending and rotation of the back. Case 1 revealed that sagittal plane angles at lumbar and thoracic spine can be analyzed throughout the motion. In Case 2, the spine rotation measurement demonstrated the capabilities of the method for determining the spinal shape in three anatomical planes.

The continuous measurement of spinal shape can be utilized in various applications. The shape of lumbar spine can be used in assessing movement control dysfunctions [159, 160]. In addition, monitoring the shape of the spine during occupational tasks could help to maintain ergonomic postures. The monitor application consisting of sensors and online analysis software could warn if unsafe postures are being adopted. Warning thresholds for the unsafe postures could be set based on movement performed according to ergonomic guidelines.

The aligning of the sensors with the vertebrae is difficult due to spinal processes. We used foamed plastic under the sensors to remove these kinds of artefacts. The calibration method handles the alignment problem by utilizing a neutral standing posture. The misalignment measured at the neutral posture is removed from the data at every time step. The assumed spine posture at calibration can be adjusted in a subject-specific manner. By using sensors with smaller housing, artefacts caused by spinal processes and soft tissue deformation can be attenuated.

The camera-based motion capture suffered from errors due to the transient occlusions of the reflective markers. The comparison of the model and camera-based estimates was done graphically. The graphs can be used to analyze the reliability of both estimates. The camera setup made it possible to capture the overall 3D motion of the pelvis, spine and head. Previous validation studies have also suffered from some limitations. For example, Ha et al. [161] used separate measurements for validation, since the sensors (Fastrak®) could not be mounted simultaneously with the inertial sensors.

A few attempts have been made to determine orientations of individual vertebrae based on orientations measured on the skin. Berthonnaud et al. [162] extracted the lordosis and kyphosis curves of spine and back surface profiles from radiographs. They fitted b-splines to the curves and constructed subject-specific transfer functions between the internal and external curves, they found large inter-subject (N=16) variability. The ratio of internal and the external lordosis of the lumbar spine varied between 0.88 and 1.31. Thus, no assumptions on the internal lordosis can be made based on those results. Campbell et al. [163] proposed a method to predict pose of lumbar vertebrae in sagittal plane noninvasively. They measured angle between S1 and T12 using a goniometer at neutral standing posture and when the upper body was bent at 30°. They validated the method using X-ray imaging, the average error of the model predictions was 3.9°. They also observed that the degree of lumbar lordosis at the neutral posture determines, at which phase of forward bending the lumbar spine in converted into kyphosis. Ma et al. [164] proposed a method for inter-vertebral angle estimation using Bayesian belief network. Their method predicts sagittal plane angles between lumbar vertebrae, the modeling required X-ray images of flexion and extension postures.

The sensor-to-sensor distances measured by cameras demonstrated that the current model estimates the distances satisfactorily. Our model could be developed further by incorporating the anatomical structures of the back into the model. The modeling of muscles, ligaments, adipose tissue, and skin could be added into the model to achieve a more realistic estimation of the distance and relative motion between the vertebra and the skin. Skin sliding could be addressed by modeling skin as an elastic sheet. The sensor positions provided by camera-based motion capture would be essential in the model development.

6.4 ROLE OF VARIOUS METHODS IN MOTION ANALYSIS

During this study, we encountered several challenges and the pros and cons of different methods in motion analysis were assessed. Motion capture using multiple cameras and reflective markers is a well-established methodology used in human motion analysis. Major issues affecting the accuracy of this method, such as camera calibration, marker placement, soft tissue motion, and marker identification were examined during this study. As long as major error sources of the method are eliminated, the accuracy of the camera-based analysis can be high. Combined with the force platform measurements, camera-based analysis remains the state-of-the-art choice for the analysis of joint loading.

State-space estimation, such as the unscented Kalman filter and smoother used in the study **II**, may be utilized in various data analysis applications [165]. For instance, Momi et al. [166] used UKF in the estimation of hip joint center location. The algorithms which combine magnetometer, accelerometer and gyroscope data to produce orientation are essential in inertial sensor measurement. These sensor fusion algorithms are often based on Kalman filter.

Inertial sensors provide the possibility for wearable whole body motion analysis. However, implementation of the motion measurements in real life faces several challenges. First, the correct functioning of the sensors in each measurement environment has to be ensured. Improper initialization of sensors or magnetic distortions caused by magnetic materials or electric fields may introduce errors in inertial sensor readings. Second, sensors should follow the orientation of the body segment. When sensors are strapped around arm and leg segment, muscle contractions cause movement artefacts.

Human motion analysis invariably has its limitations, but on the other hand, measurements of motion can produce valuable information about everyday activities without harming the subject. Commercially available motion capture devices, such as Microsoft Kinect are designed for animation and entertainment purposes. Recently, several studies have examined suitability of these devices to the motion analysis. These low-cost and easy-to-use methods can replace conventional marker-based method in some applications of motion analysis. Wearable methods, such as the one implemented in study **III** are another popular category of novel methods.

However, the modern motion laboratory equipped with a high accuracy multiple camera system and floor mounted force platforms is undoubtedly the golden standard for motion analysis measurements. Motion laboratory enables versatile validation measurements when developing novel methods. By conducting experiments in a good motion laboratory, it is possible to perform a wide variety of measurements which is essential if one wishes to develop novel methods.

7 Conclusions

The main conclusions emerging from these studies were:

1. Both hip and knee moments are reduced in proportion to the weight loss following extensive weight loss. Furthermore, the step width is reduced. The limitations noted this study acted as a stimulus to improve the methods of camera-based motion analysis for joint loading estimation.

2. The proposed method combined the UKF with a multisegment 3D model, contact constraint, and a fixed-interval smoother in a unique way. The pose of the model was defined using unit quaternions. The contact constraint was incorporated into the UKF evolution model, which enabled accurate estimates during contact events. The smoother removed the time lag from the final estimates. In the validation measurements of the method, meaningful estimates for accelerations of a rigid body and human foot were acquired during floor contact events.

3. A measurement setup and mathematical methods for the estimation of whole spine shape using wireless inertial sensors were proposed. This method can estimate spinal shape in three dimensions during unrestricted motion. The measurements showed that method is most suitable for measuring spinal shape in sagittal plane.

Bibliography

[1] K. Halvorsen, *Model-based methods in motion capture* (Acta Universitatis Upsaliensis„ 2002).

[2] T. A. Wren, G. E. Gorton, S. Ounpuu, and C. A. Tucker, “Efficacy of clinical gait analysis: a systematic review,” *Gait & posture* **34**, 149–153 (2011).

[3] S. Nadeau, M. Betschart, and F. Bethoux, “Gait analysis for poststroke rehabilitation: the relevance of biomechanical analysis and the impact of gait speed,” *Physical medicine and rehabilitation clinics of North America* **24**, 265–276 (2013).

[4] N. L. Keijsers, M. W. Horstink, and S. C. Gielen, “Movement parameters that distinguish between voluntary movements and levodopa-induced dyskinesia in Parkinsons disease,” *Human movement science* **22**, 67–89 (2003).

[5] Y. Barak, R. C. Wagenaar, and K. G. Holt, “Gait characteristics of elderly people with a history of falls: a dynamic approach,” *Physical therapy* **86**, 1501–1510 (2006).

[6] T. Liikavainio, T. Bragge, M. Hakkarainen, P. A. Karjalainen, and J. P. Arokoski, “Gait and muscle activation changes in men with knee osteoarthritis,” *The Knee* **17**, 69–76 (2010).

[7] D. Bytyqi, B. Shabani, S. Lustig, L. Cheze, N. K. Gjurgjeala, and P. Neyret, “Gait knee kinematic alterations in medial osteoarthritis: three dimensional assessment,” *International orthopaedics* **38**, 1191–1198 (2014).

[8] R. J. Leigh, S. T. Osis, and R. Ferber, “Kinematic gait patterns and their relationship to pain in mild-to-moderate hip osteoarthritis,” *Clinical Biomechanics* **34**, 12–17 (2016).

[9] T. D. V. Cooke, E. A. Sled, and R. A. Scudamore, “Frontal plane knee alignment: a call for standardized measurement,” *Journal of Rheumatology* **34**, 1796–1801 (2007).

[10] J. L. McGinley, R. Baker, R. Wolfe, and M. E. Morris, “The reliability of three-dimensional kinematic gait measurements: a systematic review,” *Gait & posture* **29**, 360–369 (2009).

[11] O. Schipplein and T. Andriacchi, “Interaction between active and passive knee stabilizers during level walking,” *Journal of Orthopaedic Research* **9**, 113–119 (1991).

[12] K. L. Bennell, M. Kyriakides, B. Metcalf, T. Egerton, T. V. Wrigley, P. W. Hodges, M. A. Hunt, E. M. Roos, A. Forbes, E. Ageberg, et al., “Neuromuscular versus quadriceps strengthening exercise in patients with medial knee osteoarthritis and varus malalignment: a randomized controlled trial,” *Arthritis & Rheumatology* **66**, 950–959 (2014).

[13] J.-P. Kulmala, “The effects of locomotor pattern diversity and ageing on the lower limb joint mechanics and loading during human walking and running,” (2015).

[14] A. Baliunas, D. Hurwitz, A. Ryals, A. Karrar, J. Case, J. Block, and T. Andriacchi, “Increased knee joint loads during walking are present in subjects with knee osteoarthritis,” *Osteoarthritis and cartilage* **10**, 573–579 (2002).

[15] N. Foroughi, R. Smith, and B. Vanwanseele, “The association of external knee adduction moment with biomechanical variables in osteoarthritis: a systematic review,” *The Knee* **16**, 303–309 (2009).

[16] N. Foroughi, R. M. Smith, A. K. Lange, M. K. Baker, M. A. F. Singh, and B. Vanwanseele, “Dynamic alignment and its association with knee adduction moment in medial knee osteoarthritis,” *The Knee* **17**, 210–216 (2010).

[17] M. M. Ardestani, M. Moazen, and Z. Jin, “Sensitivity analysis of human lower extremity joint moments due to changes in joint kinematics,” *Medical engineering & physics* **37**, 165–174 (2015).

[18] M. W. Whittle, *Gait analysis: an introduction* (Butterworth-Heinemann, 2014).

[19] P. Spyropoulos, J. C. Pisciotta, K. N. Pavlou, M. A. Cairns, and S. R. Simon, “Biomechanical gait analysis in obese men,” *Arch Phys Med Rehabil* **72**, 1065–1070 (1991).

[20] B. McGraw, B. A. McClenaghan, H. G. Williams, J. Dickerson, and D. S. Ward, “Gait and postural stability in obese and nonobese prepubertal boys,” *Arch Phys Med Rehabil* **81**, 484–489 (2000).

[21] P. P. Lai, A. K. Leung, A. N. Li, and M. Zhang, “Three-dimensional gait analysis of obese adults,” *Clinical Biomechanics* **23, Supplement 1**, S2 – S6 (2008), Research and Development on Biomechanics in China.

[22] R. C. Browning and R. Kram, “Effects of obesity on the biomechanics of walking at different speeds,” *Med Sci Sports Exerc* **39**, 1632–1641 (2007).

[23] T. C. D. da Silva-Hamu, C. K. M. R. Formiga, F. M. Gervásio, D. M. Ribeiro, G. Christofoletti, and J. de França Barros, “The impact of obesity in the kinematic parameters of gait in young women,” *International journal of general medicine* **6**, 507 (2013).

[24] D. L. Gushue, J. Houck, and A. L. Lerner, “Effects of childhood obesity on three-dimensional knee joint biomechanics during walking,” *J Pediatr Orthop* **25**, 763–768 (2005).

[25] P. DeVita and T. Hortobágyi, “Obesity is not associated with increased knee joint torque and power during level walking,” *J Biomech* **36**, 1355 – 1362 (2003).

[26] S. P. Messier, “Osteoarthritis of the knee and associated factors of age and obesity: effects on gait,” *Med Sci Sports Exerc* **26**, 1446–1452 (1994).

[27] J. Nantel, M. Brochu, and F. Prince, “Locomotor Strategies in Obese and Non-obese Children,” *Obesity* **14**, 1789–1794 (2006).

[28] T. Hortobágyi, C. Herring, W. J. Pories, P. Rider, and P. DeVita, “Massive weight loss-induced mechanical plasticity in obese gait,” *J Appl Physiol* (2011).

[29] S. P. Messier, D. J. Gutekunst, C. Davis, and P. DeVita, “Weight loss reduces knee-joint loads in overweight and obese older adults with knee osteoarthritis,” *Arthritis & Rheumatism* **52**, 2026–2032 (2005).

[30] J. Aaboe, H. Bliddal, S. Messier, T. Alkjar, and M. Henriksen, “Effects of an intensive weight loss program on knee joint loading in obese adults with knee osteoarthritis,” *Osteoarthritis and Cartilage* **19**, 822 – 828 (2011).

[31] T. Lyytinen, T. Bragge, T. Liikavainio, P. Vartiainen, P. A. Karjalainen, and J. P. Arokoski, “The impact of obesity and weight loss on gait in adults,” in *The Mechanobiology of Obesity and Related Diseases* (Springer, 2014), pp. 125–147.

[32] A. W. Froehle, R. T. Laughlin, D. D. Teel II, R. J. Sherwood, and D. L. Duren, “Excess body weight loss is associated with nonpathological gait patterns in women 4 to 5 years after bariatric surgery,” *Obesity surgery* **24**, 253–259 (2014).

[33] I. L. Bacha, F. A. Benetti, and J. M. D. Greve, “Baropodometric analyses of patients before and after bariatric surgery,” *Clinics* **70**, 743–747 (2015).

[34] S. V. Gill, M. K. Walsh, J. A. Pratt, N. Toosizadeh, B. Najafi, and T. G. Travison, “Changes in spatiotemporal gait patterns during flat ground walking and obstacle crossing 1 year after bariatric surgery,” *Surgery for Obesity and Related Diseases* (2016).

[35] P. DeVita, P. Rider, and T. Hortobágyi, “Reductions in knee joint forces with weight loss are attenuated by gait adaptations in class III obesity,” *Gait & posture* **45**, 25–30 (2016).

[36] A. W. Froehle, N. Dollin, R. T. Laughlin, D. D. Teel II, R. J. Sherwood, and D. L. Duren, “Bariatric surgery: Effects on patient gait and function,” `http://lermagazine.com/article/bariatric-surgery-effects-on-patient-gait-and-function`, date retrieved 23 December 2016 (2014).

[37] S. Springer and G. Yogev Seligmann, “Validity of the Kinect for Gait Assessment: A Focused Review,” *Sensors* **16**, 194 (2016).

[38] H. K. Vincent, K. Ben-David, B. P. Conrad, K. M. Lamb, A. N. Seay, and K. R. Vincent, “Rapid changes in gait, musculoskeletal pain, and quality of life after bariatric surgery,” *Surgery for Obesity and Related Diseases* **8**, 346–354 (2012).

[39] A. Peters, B. Galna, M. Sangeux, M. Morris, and R. Baker, “Quantification of soft tissue artifact in lower limb human motion analysis: a systematic review,” *Gait & posture* **31**, 1–8 (2010).

[40] M. S. Andersen, M. Damsgaard, J. Rasmussen, D. K. Ramsey, and D. L. Benoit, "A linear soft tissue artefact model for human movement analysis: proof of concept using in vivo data," *Gait & posture* **35**, 606–611 (2012).

[41] M. Akbarshahi, A. G. Schache, J. W. Fernandez, R. Baker, S. Banks, and M. G. Pandy, "Non-invasive assessment of soft-tissue artifact and its effect on knee joint kinematics during functional activity," *Journal of biomechanics* **43**, 1292–1301 (2010).

[42] S. Mahallati, H. Rouhani, R. Preuss, K. Masani, and M. R. Popovic, "Multisegment Kinematics of the Spinal Column: Soft Tissue Artifacts Assessment," *Journal of biomechanical engineering* **138**, 071003 (2016).

[43] Y. Blache, R. Dumas, A. Lundberg, and M. Begon, "Main component of soft tissue artifact of the upper-limbs with respect to different functional, daily life and sports movements," *Journal of Biomechanics* (2016).

[44] R. Stagni, S. Fantozzi, A. Cappello, and A. Leardini, "Quantification of soft tissue artefact in motion analysis by combining 3D fluoroscopy and stereophotogrammetry: a study on two subjects," *Clinical Biomechanics* **20**, 320–329 (2005).

[45] M. Kozanek, A. Hosseini, F. Liu, S. K. V. de Velde, T. J. Gill, H. E. Rubash, and G. Li, "Tibiofemoral kinematics and condylar motion during the stance phase of gait," *Journal of Biomechanics* **42**, 1877 – 1884 (2009).

[46] S. P. Hacker, A. Ignatius, and L. Dürselen, "The influence of the test setup on knee joint kinematics - A meta-analysis of tibial rotation," *Journal of Biomechanics* (2016).

[47] L. Herda, *Using biomechanical constraints to improve video-based motion capture*, PhD thesis (EPFL, 2003).

[48] P. Cerveri, A. Pedotti, and G. Ferrigno, "Robust recovery of human motion from video using Kalman filters and virtual humans," *Human Movement Science* **22**, 377–404 (2003).

[49] J. del Rincon, D. Makris, C. Uruñuela, and J.-C. Nebel, "Tracking Human Position and Lower Body Parts Using Kalman and Particle Filters Constrained by Human Biomechanics," *Systems, Man, and Cybernetics, Part B: Cybernetics, IEEE Transactions on* **41**, 26–37 (2011).

[50] K. Halvorsen, "Using an Extended Kalman Filter for Rigid Body Pose Estimation," *Journal of Biomechanical Engineering* **127** (2005).

[51] R. E. Kalman, "A New Approach to Linear Filtering and Prediction Problems," *Journal of Basic Engineering* **83**, 35–45 (1960).

[52] P. Cerveri, A. Pedotti, and G. Ferrigno, "Kinematical models to reduce the effect of skin artifacts on marker-based human motion estimation," *Journal of Biomechanics* **38**, 2228–2236 (2005).

[53] H. E. Rauch, F. Tung, and C. T. Striebel, "Maximum likelihood estimates of linear dynamic systems," *AIAA Journal* **3**, 1445–1450 (1965).

[54] F. D. Groote, T. D. Laet, I. Jonkers, and J. D. Schutter, "Kalman smoothing improves the estimation of joint kinematics in marker-based human gait analysis," *Journal of Biomechanics* **41**, 3390–3398 (2008).

[55] K. Dorfmüller-Ulhaas, "Robust optical user motion tracking using a kalman filter," in *10th ACM Symposium on Virtual Reality Software and Technology* (2003).

[56] B. A. MacWilliams, "A comparison of four functional methods to determine centers and axes of rotations," *Gait & Posture* **28**, 673–679 (2008).

[57] V. Camomilla, A. Cereatti, G. Vannozzi, and A. Cappozzo, "An optimized protocol for hip joint centre determination using the functional method," *Journal of biomechanics* **39**, 1096–1106 (2006).

[58] K. A. Ball and T. M. Greiner, "A procedure to refine joint kinematic assessments: Functional Alignment," *Computer methods in biomechanics and biomedical engineering* **15**, 487–500 (2012).

[59] L.-P. Rivest, S. Baillargeon, and M. Pierrynowski, "A directional model for the estimation of the rotation axes of the ankle joint," *Journal of the American Statistical Association* (2012).

[60] R. Hartley and A. Zisserman, *Multiple view geometry in computer vision* (Cambridge university press, 2003).

[61] T. Bragge, *Component based signal prediction in motion analysis*, MSc thesis (University of Kuopio, 2007).

[62] K. Saber-Sheikh, E. C. Bryant, C. Glazzard, A. Hamel, and R. Y. W. Lee, "Feasibility of using inertial sensors to assess human movement," *Manual therapy* **15**, 122–125 (2010).

[63] C. Duc, P. Salvia, A. Lubansu, V. Feipel, and K. Aminian, "A wearable inertial system to assess the cervical spine mobility: comparison with an optoelectronic-based motion capture evaluation," *Medical engineering physics* **36**, 49–56 (2014).

[64] R. Zemp, R. List, T. Gülay, J. P. Elsig, J. Naxera, W. R. Taylor, and S. Lorenzetti, "Soft Tissue Artefacts of the Human Back: Comparison of the Sagittal Curvature of the Spine Measured Using Skin Markers and an Open Upright MRI," *PloS one* **9**, e95426 (2014).

[65] E. Charry, M. Umer, and S. Taylor, "Design and validation of an ambulatory inertial system for 3-D measurements of low back movements," in *Intelligent Sensors, Sensor Networks and Information Processing (ISSNIP), 2011 Seventh International Conference on* (IEEE, 2011), pp. 58–63.

[66] H. Kim, S. H. Shin, J. K. Kim, Y. J. Park, H. S. Oh, and Y. B. Park, "Cervical coupling motion characteristics in healthy people using a wireless inertial measurement unit," *Evid Based Complement Alternat Med* **2013**, 570428 (2013).

[67] W.-S. Yun, H. Kim, J. H. Ahn, Y.-B. Park, and Y.-J. Park, "Individual characteristics of reliable lumbar coupling motions," *European Spine Journal* **24**, 1917–1925 (2015).

[68] T. Ishii, Y. Mukai, N. Hosono, H. Sakaura, R. Fujii, Y. Nakajima, S. Tamura, K. Sugamoto, and H. Yoshikawa, "Kinematics of the subaxial cervical spine in rotation in vivo three-dimensional analysis," *Spine* **29**, 2826–2831 (2004).

[69] A. Chhikara, A. H. McGregor, L. Hadjilucas, F. Bello, and A. S. Rice, "Quantitative assessment of the motion of the lumbar spine and pelvis with wearable inertial sensors," in *Body Sensor Networks (BSN), 2010 International Conference on* (IEEE, 2010), pp. 9–15.

[70] T. Consmüller, A. Rohlmann, D. Weinland, C. Druschel, G. N. Duda, and W. R. Taylor, "Comparative evaluation of a novel measurement tool to assess lumbar spine posture and range of motion," *European spine journal : official publication of the European Spine Society, the European Spinal Deformity Society, and the European Section of the Cervical Spine Research Society* **21**, 2170–2180 (2012).

[71] "DIERS formetric 4D analysis system," (2012), `http://www.diers.de/ProductPage.aspx?p=2` Accessed 11 November 2016.

[72] A. F. Mannion, K. Knecht, G. Balaban, J. Dvorak, and D. Grob, "A new skin-surface device for measuring the curvature and global and segmental ranges of motion of the spine: reliability of measurements and comparison with data reviewed from the literature," *European Spine Journal* **13**, 122–136 (2004).

[73] Z. Yang, J. F. Griffith, P. Leung, M. Pope, L. Sun, and R. Lee, "The accuracy of surface measurement for motion analysis of osteoporotic thoracolumbar spine," in *Engineering in Medicine and Biology Society, 2005. IEEE-EMBS 2005. 27th Annual International Conference of the* (IEEE, 2006), pp. 6871–6874.

[74] Z. Yang, H. Ma, D. Wang, and R. Lee, "Error analysis on spinal motion measurement using skin mounted sensors," in *Engineering in Medicine and Biology Society, 2008. EMBS 2008. 30th Annual International Conference of the IEEE* (IEEE, 2008), pp. 4740–4743.

[75] A. I. Cuesta-Vargas, A. Galán-Mercant, and J. M. Williams, "The use of inertial sensors system for human motion analysis," *Physical Therapy Reviews* **15**, 462–473 (2010).

[76] A. Tafazzol, N. Arjmand, A. Shirazi-Adl, and M. Parnianpour, "Lumbopelvic rhythm during forward and backward sagittal trunk rotations: Combined in vivo measurement with inertial tracking device and biomechanical modeling," *Clinical Biomechanics* **29**, 7 – 13 (2014).

[77] C. Bauer, F. Rast, M. Ernst, J. Kool, S. Oetiker, S. Rissanen, J. Suni, and M. Kankaanpää, "Concurrent validity and reliability of a novel wireless inertial measurement system to assess trunk movement," *Journal of Electromyography and Kinesiology* **25**, 782–790 (2015).

[78] C. Goodvin, E. J. Park, K. Huang, and K. Sakaki, "Development of a real-time three-dimensional spinal motion measurement system for clinical practice," *Medical and Biological Engineering and Computing* **44**, 1061–1075 (2006).

[79] J. K. Lee, G. Desmoulin, A. Khan, and E. Park, "A portable inertial sensing-based spinal motion measurement system for low back pain assessment," in *Engineering in Medicine and Biology Society, EMBC, 2011 Annual International Conference of the IEEE* (2011), pp. 4737–4740.

[80] M. Hajibozorgi and N. Arjmand, "Sagittal range of motion of the thoracic spine using inertial tracking device and effect of measurement errors on model predictions," *Journal of biomechanics* **49**, 913–918 (2016).

[81] G. Bellusci, F. Dijkstra, and P. Slycke, "Xsens MTw: Miniature Wireless Inertial Motion Tracker for Highly Accurate 3D Kinematic Applications," *Xsens Technologies* (2013).

[82] M. Cognolato, *Experimental validation of Xsens inertial sensors during clinical and sport motion capture applications*, PhD thesis (University of Padova, 2012).

[83] M. Jäger, C. Jordan, A. Theilmeier, N. Wortmann, S. Kuhn, A. Nienhaus, and A. Luttmann, "Lumbar-load analysis of manual patient-handling activities for biomechanical overload prevention among healthcare workers," *Annals of occupational hygiene* **57**, 528–544 (2013).

[84] T. B. Moeslund, A. Hilton, and V. Krüger, "A survey of advances in vision-based human motion capture and analysis," *Computer vision and image understanding* **104**, 90–126 (2006).

[85] R. Poppe, "Vision-based human motion analysis: An overview," *Computer vision and image understanding* **108**, 4–18 (2007).

[86] A. Laurentini, "The visual hull concept for silhouette-based image understanding," *IEEE Transactions on pattern analysis and machine intelligence* **16**, 150–162 (1994).

[87] S. Corazza, L. Muendermann, A. Chaudhari, T. Demattio, C. Cobelli, and T. P. Andriacchi, "A markerless motion capture system to study musculoskeletal biomechanics: visual hull and simulated annealing approach," *Annals of biomedical engineering* **34**, 1019–1029 (2006).

[88] E. Ceseracciu, Z. Sawacha, and C. Cobelli, "Comparison of markerless and marker-based motion capture technologies through simultaneous data collection during gait: proof of concept," *PloS one* **9**, e87640 (2014).

[89] L. Becker and P. Russ, "Evaluation of joint angle accuracy using markerless silhouette based tracking and hybrid tracking against traditional marker tracking," *Poster für Masterarbeit bei Simi Reality Motion Systems GmbH und der Otto-von-Guericke-Universität Magdeburg* (2015).

[90] M. A. Perrott, T. Pizzari, J. Cook, and J. A. McClelland, "Comparison of lower limb and trunk kinematics between markerless and marker-based motion capture systems," *Gait & Posture* **52**, 57–61 (2017).

[91] V. Ganapathi, C. Plagemann, D. Koller, and S. Thrun, "Real time motion capture using a single time-of-flight camera," in *Computer Vision and Pattern Recognition (CVPR), 2010 IEEE Conference on* (IEEE, 2010), pp. 755–762.

[92] A. Muro-de-la Herran, B. Garcia-Zapirain, and A. Mendez-Zorrilla, "Gait analysis methods: an overview of wearable and non-wearable systems, highlighting clinical applications," *Sensors* **14**, 3362–3394 (2014).

[93] J. MacCormick, "How does the Kinect work?," (2012), Accessed 03 January 2017.

[94] R. A. Clark, Y.-H. Pua, A. L. Bryant, and M. A. Hunt, "Validity of the Microsoft Kinect for providing lateral trunk lean feedback during gait retraining," *Gait & posture* **38**, 1064–1066 (2013).

[95] M. Huber, A. Seitz, M. Leeser, and D. Sternad, "Validity and reliability of Kinect skeleton for measuring shoulder joint angles: a feasibility study," *Physiotherapy* **101**, 389 – 393 (2015).

[96] B. Bonnechére, B. Jansen, P. Salvia, H. Bouzahouene, L. Omelina, F. Moiseev, V. Sholukha, J. Cornelis, M. Rooze, and S. V. S. Jan, "Validity and reliability of the Kinect within functional assessment activities: Comparison with standard stereophotogrammetry," *Gait Posture* **39**, 593 – 598 (2014).

[97] M. Gabel, R. Gilad-Bachrach, E. Renshaw, and A. Schuster, “Full body gait analysis with Kinect,” in *2012 Annual International Conference of the IEEE Engineering in Medicine and Biology Society* (IEEE, 2012), pp. 1964–1967.

[98] A. Pfister, A. M. West, S. Bronner, and J. A. Noah, “Comparative abilities of Microsoft Kinect and Vicon 3D motion capture for gait analysis,” *Journal of medical engineering & technology* **38**, 274–280 (2014).

[99] X. Xu, R. W. McGorry, L.-S. Chou, J.-h. Lin, and C.-c. Chang, “Accuracy of the Microsoft Kinect for measuring gait parameters during treadmill walking,” *Gait & posture* **42**, 145–151 (2015).

[100] X. Xu and R. W. McGorry, “The validity of the first and second generation Microsoft Kinect for identifying joint center locations during static postures,” *Applied Ergonomics* **49**, 47 – 54 (2015).

[101] R. A. Clark, Y.-H. Pua, C. C. Oliveira, K. J. Bower, S. Thilarajah, R. McGaw, K. Hasanki, and B. F. Mentiplay, “Reliability and concurrent validity of the Microsoft Xbox One Kinect for assessment of standing balance and postural control,” *Gait Posture* **42**, 210 – 213 (2015).

[102] R. P. Kuster, B. Heinlein, C. M. Bauer, and E. S. Graf, “Accuracy of KinectOne to quantify kinematics of the upper body,” *Gait & posture* **47**, 80–85 (2016).

[103] D. J. Geerse, B. H. Coolen, and M. Roerdink, “Kinematic Validation of a Multi-Kinect v2 Instrumented 10-Meter Walkway for Quantitative Gait Assessments,” *PloS one* **10**, e0139913 (2015).

[104] B. F. Mentiplay, L. G. Perraton, K. J. Bower, Y.-H. Pua, R. McGaw, S. Heywood, and R. A. Clark, “Gait assessment using the Microsoft Xbox One Kinect: Concurrent validity and inter-day reliability of spatiotemporal and kinematic variables,” *Journal of biomechanics* **48**, 2166–2170 (2015).

[105] M. Eltoukhy, J. Oh, C. Kuenze, and J. Signorile, “Improved kinect-based spatiotemporal and kinematic treadmill gait assessment,” *Gait & Posture* **51**, 77–83 (2017).

[106] L. Yang, B. Yang, H. Dong, and A. E. Saddik, “3-D Markerless Tracking of Human Gait by Geometric Trilateration of Multiple Kinects,” *IEEE Systems Journal* (2016).

[107] J. Stuhmer, S. Nowozin, A. Fitzgibbon, R. Szeliski, T. Perry, S. Acharya, D. Cremers, and J. Shotton, “Model-Based Tracking at 300Hz using Raw Time-of-Flight Observations,” in *Proceedings of the IEEE International Conference on Computer Vision* (2015), pp. 3577–3585.

[108] D. Webster and O. Celik, “Systematic review of Kinect applications in elderly care and stroke rehabilitation,” *Journal of neuroengineering and rehabilitation* **11**, 1 (2014).

[109] E. E. Stone and M. Skubic, “Fall detection in homes of older adults using the Microsoft Kinect,” *IEEE journal of biomedical and health informatics* **19**, 290–301 (2015).

[110] D. Levac, D. Espy, E. Fox, S. Pradhan, and J. E. Deutsch, “Kinect-ing with clinicians: a knowledge translation resource to support decision making about video game use in rehabilitation,” *Physical therapy* (2014).

[111] Intel RealSense, “Intel RealSense — Wikipedia, The Free Encyclopedia,” (2016), Accessed 03 January 2017.

[112] “Intel RealSense product page,” (2017), `https://software.intel.com/en-us/realsense/home` Accessed 03 January 2017.

[113] A. K. Bhowmik, “35-1: Invited Paper: Real-Time 3D-Sensing Technologies and Applications in Interactive and Immersive Devices,” in *SID Symposium Digest of Technical Papers*, Vol. 47 (Wiley Online Library, 2016), pp. 440–443.

[114] M.-A. Wallius, S. M. Rissanen, T. Bragge, P. Vartiainen, P. A. Karjalainen, K. RÄSÄNEN, and S. JÄRVELIN-PASANEN, “Effects of mop handle height on shoulder muscle activity and perceived exertion during floor mopping using a figure eight method,” *Industrial health* **54**, 58 (2016).

[115] M. C. Schall Jr, N. B. Fethke, H. Chen, S. Oyama, and D. I. Douphrate, “Accuracy and repeatability of an inertial measurement unit system for field-based occupational studies,” *Ergonomics* 1–12 (2015).

[116] M. Iosa, P. Picerno, S. Paolucci, and G. Morone, “Wearable inertial sensors for human movement analysis,” *Expert review of medical devices* **13**, 641–659 (2016).

[117] M. Supej, “3D measurements of alpine skiing with an inertial sensor motion capture suit and GNSS RTK system,” *Journal of Sports Sciences* **28**, 759–769 (2010).

[118] A. Krüger and J. Edelmann-Nusser, “Biomechanical analysis in freestyle snowboarding: application of a full-body inertial measurement system and a bilateral insole measurement system,” *Sports Technology* **2**, 17–23 (2009).

[119] J. Chardonnens, J. Favre, F. Cuendet, G. Gremion, and K. Aminian, “Measurement of the dynamics in ski jumping using a wearable inertial sensor-based system,” *Journal of sports sciences* **32**, 591–600 (2014).

[120] G. Logar and M. Munih, “Estimation of Joint Forces and Moments for the In-Run and Take-Off in Ski Jumping Based on Measurements with Wearable Inertial Sensors,” *Sensors* **15**, 11258–11276 (2015).

[121] F. A. d. Magalhaes, G. Vannozzi, G. Gatta, and S. Fantozzi, “Wearable inertial sensors in swimming motion analysis: a systematic review,” *Journal of sports sciences* **33**, 732–745 (2015).

[122] K. J. ODonovan, R. Kamnik, D. T. OKeeffe, and G. M. Lyons, “An inertial and magnetic sensor based technique for joint angle measurement,” *Journal of biomechanics* **40**, 2604–2611 (2007).

[123] I. Lihinikaduarachchi, S. A. Rajapaksha, C. Saumya, V. Senevirathne, and P. Silva, “Inertial Measurement units based wireless sensor network for real time gait analysis,” in *TENCON 2015-2015 IEEE Region 10 Conference* (IEEE, 2015), pp. 1–6.

[124] G. Faber, C. Chang, I. Kingma, J. Dennerlein, and J. van Die “Estimating 3D L5/S1 moments and ground reaction forces during trunk bending using a full-body ambulatory inertial motion capture system,” *Journal of Biomechanics* **49**, 904 – 912 (2016), SI: Spine Loading and Deformation.

[125] J.-T. Zhang, A. C. Novak, B. Brouwer, and Q. Li, “Concurrent validation of Xsens MVN measurement of lower limb joint angular kinematics,” *Physiological measurement* **34**, N63 (2013).

[126] I. H. López-Nava, I. González, A. Muñoz-Meléndez, and J. Bravo, “Comparison of a Vision-Based System and a Wearable Inertial-Based System for a Quantitative Analysis and Calculation of Spatio-Temporal Parameters,” in *Ambient Intelligence for Health* (Springer, 2015), pp. 116–122.

[127] L. Ren, R. Jones, and D. Howard, “Whole body inverse dynamics over a complete gait cycle based only on measured kinematics,” *Journal of Biomechanics* **41**, 2750–2759 (2008).

[128] T. Sim, H. Kwon, S. E. Oh, S.-B. Joo, A. Choi, H. M. Heo, K. Kim, and J. H. Mun, “Predicting Complete Ground Reaction Forces and Moments During Gait With Insole Plantar Pressure Information Using a Wavelet Neural Network,” *Journal of biomechanical engineering* **137**, 091001 (2015).

[129] M. J. Hakkarainen, T. Bragge, T. Liikavainio, J. Arokoski, P. A. Karjalainen, and M. Tarvainen, “Method for testing motion analysis laboratory measurement systems,” *Journal of biomechanical engineering* **132**, 114501 (2010).

[130] T. Liikavainio, T. Bragge, M. Hakkarainen, J. S. Jurvelin, P. A. Karjalainen, and J. P. Arokoski, “Reproducibility of Loading Measurements With Skin-Mounted Accelerometers During Walking,” *Archives of Physical Medicine and Rehabilitation* **88**, 907 – 915 (2007).

[131] P. Vartiainen, T. Bragge, T. Lyytinen, M. Hakkarainen, P. A. Karjalainen, and J. P. Arokoski, “Kinematic and kinetic changes in obese gait in bariatric surgery-induced weight loss,” *Journal of Biomechanics* **45**, 1769 – 1774 (2012).

[132] D. Eberly, “Quaternion Algebra and Calculus,” `http://www.geometrictools.com/Documentation/Quaternions.pdf` Accessed 13 June 2016 (2008).

[133] K. Shoemake, “Animating rotation with quaternion curves,” in *ACM SIGGRAPH computer graphics*, Vol. 19 (ACM, 1985), pp. 245–254.

[134] E. Kraft, “A quaternion-based unscented Kalman filter for orientation tracking,” in *Information Fusion, 2003. Proceedings of the Sixth International Conference of*, Vol. 1 (2003), pp. 47 –54.

[135] N. Bellamy, W. W. Buchanan, C. H. Goldsmith, J. Campbell, and L. W. Stitt, “Validation study of WOMAC: a health status instrument for measuring clinically important patient relevant outcomes to antirheumatic drug therapy in patients with osteoarthritis of the hip or knee.,” *Journal of Rheumatology* **15**, 1833–1840 (1988).

[136] J. H. Kellgren, M. R. Jeffrey, and J. Ball, *The epidemiology of chronic rheumatism. Atlas of standard radiographs of arthritis.* (F. A. Davis, 1963).

[137] B. M. Nigg and W. Herzog, *BIOMECHANICS of the Musculo-skeletal System*, Second ed. (Wiley, 1999).

[138] S. J. Julier and J. K. Uhlmann, “A new extension of the Kalman filter to nonlinear systems,” in *International Symposium on Aerospace/Defense Sensing, Simulation and Controls* (1997).

[139] S. Särkkä, “Unscented Rauch–Tung–Striebel Smoother,” *IEEE TRANSACTIONS ON AUTOMATIC CONTROL* **53**, 845–848 (2008).

[140] J. Hartikainen and S. Särkkä, “Optimal filtering with Kalman filters and smoothers - a Manual for Matlab toolbox EKF/UKF,” (2008).

[141] X. Rong Li and V. Jilkov, “Survey of maneuvering target tracking. Part I. Dynamic models,” *Aerospace and Electronic Systems, IEEE Transactions on* **39**, 1333 – 1364 (2003).

[142] Y. Bar-Shalom and X.-R. Li, *Estimation and Tracking: Principles, Techniques, and Software* (Artech House, 1993).

[143] M. Ernst, F. Rast, C. Bauer, V. Marcar, and J. Kool, “Determination of thoracic and lumbar spinal processes by their percentage position between C7 and the PSIS level,” *BMC Research Notes* **6**, 58 (2013).

[144] G. Wu, S. Siegler, P. Allard, C. Kirtley, A. Leardini, D. Rosenbaum, M. Whittle, D. D DLima, L. Cristofolini, H. Witte, et al., “ISB recommendation on definitions of joint coordinate system of various joints for the reporting of human joint motion–part I: ankle, hip, and spine,” *Journal of biomechanics* **35**, 543–548 (2002).

[145] R. Dumas, L. Chèze, and J.-P. Verriest, “Adjustments to McConville et al. and Young et al. body segment inertial parameters,” *Journal of Biomechanics* **40**, 543–553 (2007).

[146] “OpenSim software,” (2015), `https://simtk.org/home/opensim` Accessed 29 June 2016.

[147] A. Hof, C. Koerhuis, and J. Winters, “‘Coupled motions’ in cervical spine rotation can be misleading. Comment on V. Feipel, B. Rondelet, J.-P. Le Pallec and M. Rooze. Normal global motion of the cervical spine: an electrogoniometric study. Clin. Biomechanics 1999; 14: 462–470,” *Clinical Biomechanics* **16**, 455 – 456 (2001).

[148] Xsens Technologies, “MTw User Manual,” (2013), `http://www.xsens.com/download/usermanual/MTw_usermanual.pdf` Accessed 29 June 2016.

[149] D. Roetenberg, H. Luinge, and P. Slycke, “Xsens MVN: full 6DOF human motion tracking using miniature inertial sensors,” *Xsens Motion Technologies BV, Tech. Rep* (2009).

[150] S. Messier, C. Legault, R. Loeser, S. V. Arsdale, C. Davis, W. Ettinger, and P. DeVita, “Does high weight loss in older adults with knee osteoarthritis affect bone-on-bone joint loads and muscle forces during walking?,” *Osteoarthritis and Cartilage* **19**, 272 – 280 (2011).

[151] R. W. Bohannon and A. W. Andrews, “Normal walking speed: a descriptive meta-analysis,” *Physiotherapy* **97**, 182 – 189 (2011).

[152] L. Ren, R. K. Jones, and D. Howard, “Whole body inverse dynamics over a complete gait cycle based only on measured kinematics,” *Journal of biomechanics* **41**, 2750–2759 (2008).

[153] M. A. Lafortune, E. Henning, and G. A. Valiant, “Tibial shock measured with bone and skin mounted transducers,” *Journal of Biomechanics* **28**, 989 – 993 (1995).

[154] R. W. Bisseling and A. L. Hof, “Handling of impact forces in inverse dynamics,” *Journal of biomechanics* **39**, 2438–2444 (2006).

[155] E. Kristianslund, T. Krosshaug, and A. J. Van den Bogert, “Effect of low pass filtering on joint moments from inverse dynamics: implications for injury prevention,” *Journal of biomechanics* **45**, 666–671 (2012).

[156] T. E. Hewett, G. D. Myer, B. D. Roewer, and K. R. Ford, “Letter to the editor regarding ”Effect of low pass filtering on joint moments from inverse dynamics: implications for injury prevention”,” *Journal of biomechanics* **45**, 2058–2059 (2012).

[157] T. D. Collins, S. N. Ghoussayni, D. J. Ewins, and J. A. Kent, “A six degrees-of-freedom marker set for gait analysis: repeatability and comparison with a modified Helen Hayes set,” *Gait & posture* **30**, 173–180 (2009).

[158] M. Żuk and C. Pezowicz, “Kinematic analysis of a six-degrees-of-freedom model based on isb recommendation: a repeatability analysis and comparison with conventional gait model,” *Applied bionics and biomechanics* (2015).

[159] H. Luomajoki, J. Kool, E. de Bruin, and O. Airaksinen, “Reliability of movement control tests in the lumbar spine,” *BMC Musculoskeletal Disorders* **8**, 90 (2007).

[160] H. Luomajoki, J. Kool, E. D. de Bruin, and O. Airaksinen, “Improvement in low back movement control, decreased pain and disability, resulting from specific exercise intervention,” *BMC Sports Science, Medicine and Rehabilitation* **2**, 1 (2010).

[161] T.-H. Ha, K. Saber-Sheikh, A. P. Moore, and M. P. Jones, “Measurement of lumbar spine range of movement and coupled motion using inertial sensors – A protocol validity study,” *Manual Therapy* **18**, 87 – 91 (2013).

[162] E. Berthonnaud, P. Fougier, R. Hilmi, H. Labelle, and J. Dimnet, “Relationship between sagittal spinal curves and back surface profiles obtained with radiographs,” *Journal of Mechanics in Medicine and Biology* **10**, 313–325 (2010).

[163] N. Campbell-Kyureghyan, M. Jorgensen, D. Burr, and W. Marras, “The prediction of lumbar spine geometry: method development and validation,” *Clinical Biomechanics* **20**, 455–464 (2005).

[164] H. T. Ma, Z. Yang, J. F. Griffith, P. C. Leung, and R. Y. Lee, “A new method for determining lumbar spine motion using Bayesian belief network,” *Medical & biological engineering & computing* **46**, 333–340 (2008).

[165] G. Ligorio and A. M. Sabatini, “A novel kalman filter for human motion tracking with an inertial-based dynamic inclinometer,” *IEEE Transactions on Biomedical Engineering* **62**, 2033–2043 (2015).

[166] E. D. Momi, E. Beretta, and G. Ferrigno, “Hip joint centre localisation with an unscented Kalman filter,” *Computer methods in biomechanics and biomedical engineering* **16**, 1319–1329 (2013).

PAAVO VARTIAINEN

Measurement and analysis of human motion provide subject-specific information about everyday movements. In addition to motion itself, the forces and torques affecting different parts of the musculoskeletal system can be assessed. In this thesis, measurement techniques and mathematical methods to determine the 3D motion of lower body and spinal column were developed and applied to estimate the loading of the knee and hip joints and the lower back.

UNIVERSITY OF
EASTERN FINLAND

uef.fi

PUBLICATIONS OF
THE UNIVERSITY OF EASTERN FINLAND
Dissertations in Forestry and Natural Sciences

ISBN 978-952-61-2478-0
ISSN 1798-5668